Available online at www.sciencedirect.com
ScienceDirect
International Journal of Solids and Structures 45 (2008) 1546–1569
INTERNATIONAL JOURNAL OF SOLIDS AND STRUCTURES
www.elsevier.com/locate/ijsolstr

# Computations of size effects in granular bodies within micro-polar hypoplasticity during plane strain compression

J. Tejchman *, J. Górski

*Faculty of Civil and Environmental Engineering, Gdańsk University of Technology, 80-952 Gdansk-Wrzeszcz, Narutowicza 11/12, Poland*

Received 16 July 2007; received in revised form 11 September 2007
Available online 22 October 2007

**Abstract**

The numerical investigations of size effects in granular bodies during a plane strain compression test are performed. To describe a mechanical behaviour of a cohesionless granular material during a monotonous deformation path in a plane strain compression test, a micro-polar hypoplastic constitutive model was used. It includes particle rotations, curvatures, non-symmetric stresses, couple stresses and the mean grain diameter as a characteristic length. In the paper, deterministic and statistical size effects in geometrically similar granular specimens are analysed. The deterministic calculations were carried out with a uniform distribution of the initial void ratio. To investigate a statistical size effect, in order to reduce the number of realizations without loosing the accuracy of the calculations, a Latin hypercube method was applied to generate Gaussian truncated random fields in a granular specimen. The results show that the statistical size effect is significantly stronger than the deterministic one. The shear resistance decreases and the rate of softening increases with increasing specimen size. The effect of the boundary roughness on shear localization is pronounced.


*Keywords:* Latin hypercube sampling; Micro-polar hypoplasticity; Plane strain compression test; Shear localization; Size effects; Void ratio

## 1. Introduction

One of the most important properties of the behaviour of many engineering materials is the size effect phenomenon, viz. experimental results vary with the size of the specimen. In the case of granular bodies, the shear resistance increases with decreasing specimen size and increasing mean grain diameter during many experiments with strain localization (Wernick, 1978; Tatsuoka et al., 1997; Tejchman and Herle, 1999; Tejchman, 2004b). Thus, results from laboratory tests which are scaled versions of the actual structures cannot be directly transferred to them. Similarly as in brittle materials (Bazant and Planas, 1998), two features can be defined: deterministic and statistical. The first one is caused by strain localization which cannot be appropriately scaled in laboratory tests. The specimen strength increases with increasing ratio $l_c/L$ ($l_c$, characteristic length of

* Corresponding author. Tel.: +48 58 347 1481; fax: +48 58 347 2044.
*E-mail addresses:* tejchmk@pg.gda.pl (J. Tejchman), jgorski@pg.gda.pl (J. Górski).

0020-7683/$ - see front matter © 2007 Elsevier Ltd. All rights reserved.
doi:10.1016/j.ijsolstr.2007.10.007

microstructure influencing both the thickness and spacing of strain localization; $L$, specimen size). This feature is strongly influenced by the pressure level (Tatsuoka et al., 1997); friction ratio and dilatancy decrease with increasing pressure. A statistical (or stochastic) effect is caused by the spatial randomness of material properties. According to Weibull's (1951) theory, this effect is caused by weak spots whose relative amount usually grows with increasing specimen size. Thus, the strength diminishes with increasing specimen size. Up to now, such size effects are not taken into account in the specifications like design codes for engineering structures. The physical understanding of size effects is of major importance for civil engineers who try to extrapolate experimental outcomes at laboratory scale to results which can be used in big scale situations. Since large geosystems or structures are beyond the range of testing in laboratories their design has to rely on a realistic extrapolation of testing results with smaller size.

In the case of granular materials involving shear localization, empirical size effect laws are not known as the performance of laboratory tests with large specimens is more complex than in brittle solids. In addition, the effect of pressure is more pronounced. Deterministic size effects have already been studied in granular materials using a FEM based on enhanced continua including a characteristic length for a kind of micro-structure (e,g. Maier, 2002; Tejchman, 2004a), and by a strong discontinuity approach (Regueiro and Borja, 2001) whereas statistical size effects have rarely been simulated (Gutierrez and de Borst, 1998; Gutierrez, 2006; Niemunis et al., 2005).

For brittle materials are only few reliable approaches to the size effect. For example, two deterministic size effects proposed by Bazant (Bazant and Planas, 1998) for geometrically similar structures allow to take into account a size difference by determining the tensile strength of pre-notched structures and structures without an initial crack. The material strength is bound for small sizes by a plasticity limit whereas for large sizes the material follows linear elastic fracture mechanics. The most known statistical effect is the already mentioned Weibull's (1951) theory (called also the weakest link theory) which is based on a distribution of flaws in materials. It postulates that a structure is as strong as its weakest component. The structure fails when its strength is exceeded, since a stress redistribution is not considered. This model is not able to account for a spatial correlation between local material properties.

The intention of the numerical simulations for this paper is to investigate deterministic and statistical size effects (expressed by the specimen size and the distribution of the initial void ratio) in cohesionless granular materials like sand by considering the influence of shear localization under quasi-static conditions on the peak shear resistance and at residual states. In the calculations, attention was laid on the effect of a stochastic distribution of the initial void ratio on the shear zone formation. Size effects were investigated only for a plane strain compression test under constant lateral pressure, which is an important test to investigate granular materials (Vardoulakis, 1977; Vardoulakis et al., 1978; Desrues and Viggiani, 2004). A finite element method with a micro-polar hypoplastic constitutive model (Tejchman and Gudehus, 2001; Tejchman and Niemunis, 2006) was used which is able to describe the essential properties of granular bodies during shear localization in a wide range of pressures and densities during monotonous deformation paths. Various properties of granular bodies may be considered as randomly distributed. In the present work, for the sake of simplicity, only fluctuations of void ratio are of primary interest as proposed by Gudehus and Nübel (2004). Deterministic plane strain calculations were performed with a uniform distribution of the initial void ratio in dense sand for six geometrically similar specimens of different sizes. The statistical size effect analyses were carried out with spatially correlated homogeneous distributions of an initial void ratio for two specimen sizes of dense sand. The effect of boundary roughness on size effects and shear localization was also investigated. Truncated Gaussian random fields were generated using a conditional rejection method (Walukiewicz et al., 1997) for weakly and strongly correlated random fields. The approximated results were obtained using a Latin hypercube sampling method (Bazant and Lin, 1985; Florian, 1992) belonging to a group of reduced Monte Carlo Methods (Hurtado and Barbat, 1998). This approach enables a significant reduction of the sample number without loosing the accuracy of calculations. Due to the lack of experimental data with respect to the specimen size and statistical distribution of the initial void ratio, the FE-results have not been compared with laboratory tests except of results for the specimen size of $40 \times 140\ \mathrm{mm}^2$ which were confronted with corresponding laboratory experiments performed by Vardoulakis (1977) and Vardoulakis et al. (1978). It should be pointed out that our analysis can be considered as a preliminary one and no general conclusions in the context of usefulness to practice

can be formulated yet since our calculations were carried out only for geometrically similar specimens and the effect of varying pressure was not taken into account.

This paper continues the papers presented by Tejchman and Górski (2007a,b). In the first paper (Tejchman and Górski, 2007a), deterministic and statistical size effects were investigated during quasi-static shearing of an infinite granular layer between two very rough boundaries under constant vertical pressure using the direct Monte Carlo method and two reduction approaches: stratified sampling and Latin hypercube sampling. The calculations have shown that the solution of nonlinear problems with random distributions on the basis of several samples is feasible. The deterministic size effect was rather small. The shear resistance at peak and at residual state decreased slightly with increasing ratio of the layer height $h_0$ and mean grain diameter $d_{50}$. However, the material ductility defined as the ratio between the energy consumed during shearing after and before the peak strongly increased with decreasing $h_0/d_{50}$. The mean shear resistance at peak with random void ratios was always smaller than this with the same initial mean void ratio. It diminished with increasing $h_0/d_{50}$. Thus, the statistical size effect was stronger than the deterministic one. In turn, in the second paper (Tejchman and Górski, 2007b), calculations with deterministic and statistical size effect were performed in granular specimens subject to plane strain compression. To estimate the statistical size effect, only Latin hypercube sampling was used. The deterministic size effect turned out again smaller than the statistical one. As compared to the FE-results published by Tejchman and Górski (2007b), the innovations in the present paper are the following: (a) to reduce the effect of the element mesh dimensions, a local average procedure was additionally applied, (b) the effect of the roughness of the top and bottom boundary on size effects was studied, and (c) the influence of the standard deviation and correlation range on the shearing resistance was investigated.

The effect of the distribution of the initial void ratio on the sand behaviour during a plane strain compression test has been already performed by Gudehus and Nübel (2004). However, a spatial correlation of the initial void ratio was ignored in their calculations.

The outline of the present paper is as follows. First, the employed micro-polar hypoplastic model is briefly summarized (Section 2). Then, the simulation of discrete random fields is described. Information about the finite element discretisation and boundary conditions are given in Section 3. The numerical results of the deterministic and statistical size effects are discussed in Section 4. Conclusions are listed in Section 5.

## 2. Micro-polar hypoplastic model

Granular materials consist of grains in contact, and of voids. Their micromechanical behaviour is inherently discontinuous, heterogeneous and non-linear. Despite the discrete nature of granular materials, their mechanical behaviour can be reasonably described by continuum models, in particular elastoplastic (Lade, 1977; Vermeer, 1982; Pestana and Whittle, 1999; Hattamleh et al., 2005) and hypoplastic ones (Kolymbas, 1977; Desrues and Chambon, 1989; Wu, 1992; Darve et al., 1995). Non-polar hypoplastic constitutive models formulated at Karlsruhe University (Gudehus, 1996; Bauer, 1996; von Wolffersdorff, 1996) describe the evolution of the effective stress tensor depending on the current void ratio, stress state and rate of deformation by isotropic non-linear tensorial functions according to a representation theorem by Wang (1970). These constitutive models were formulated by a heuristic process considering the essential mechanical properties of granular materials undergoing homogeneous deformations. A striking feature of hypoplasticity is that the stress rate is homogeneous of order 1 in the deformation rate. Hypoplastic models are capable of describing a number of significant properties of granular materials: non-linear stress–strain relationship, dilatant and contractant behaviour, pressure dependence, density dependence and material softening. A further feature of hypoplastic models is the inclusion of critical states, i.e. states in which a grain aggregate can deform continuously be deformed at constant stress and constant volume. In contrast to elasto-plastic models, a decomposition of deformation components into elastic and plastic parts, the formulation of a yield surface, plastic potential, flow rule and hardening rule are not needed. The hallmark of these models is their simple formulation and procedure for determining material parameters with standard laboratory experiments. The material parameters are related to granulometric properties, viz. size distribution, shape, angularity and hardness of grains (Herle and Gudehus, 1999). A further advantage lies in the fact that one single set of material parameters is valid for a wide range of pressures and densities. An exhaustive review of the development of hypoplasticity can be found in Wu and Kolymbas (2000) and Tamagnini et al. (2000). To increase the

application range, a hypoplastic constitutive law has been extended for an elastic strain range (Niemunis and Herle, 1997), anisotropy (Tejchman et al., 2007) and for viscosity (Niemunis, 2003; Gudehus, 2006). It can be also used for soils with low friction angles (Herle and Kolymbas, 2004) and clays (Masin, 2005).

Hypoplastic constitutive models without a characteristic length can describe realistically the onset of shear localization, but not its further evolution (Maier, 2002). A characteristic length can be introduced into hypoplasticity by means of micro-polar, non-local or second-gradient theories (Maier, 2002; Tejchman, 2004a). In this paper, a micro-polar theory was adopted (Tejchman and Wu, 1993). The micro-polar model makes use of rotations and couple stresses which have clear physical meaning for granular materials. The rotations can be observed during shearing, but remain negligible during homogeneous deformations (Oda, 1993). Pasternak and Mühlhaus (2001) have demonstrated that the additional rotational degree of freedom of a micro-polar continuum arises naturally by mathematical homogenization of an originally discrete system of spherical grains with contact forces and contact moments.

A micro-polar continuum combines two kinds of deformations at two different levels, viz: micro-rotation at the particle level and macro-deformation at the structural level (Schäfer, 1962; Mühlhaus, 1990). For the case of plane strain, each material point has three degrees of freedom: two translations and one independent rotation (Fig. 1). The gradients of the rotation are related to the curvatures, which are associated with the couple stresses. The presence of the couple stresses gives rise to a non-symmetry of the stress tensor and to a characteristic length.

The constitutive relationship between the rate of stress, the rate of couple stress, the strain rate and the curvature rate can be generally expressed by the following two equations (Tejchman and Gudehus, 2001; Tejchman and Niemunis, 2006; Tejchman and Górski, 2007a):

$$\overset{0}{\sigma}_{ij} = F_{ij}(e, \sigma_{kl}, m_i, d^c_{kl}, k_i, d_{50}) \tag{1}$$

$$\overset{0}{m}_i = G_i(e, \sigma_{kl}, m_i, d^c_{kl}, k_i, d_{50}), \tag{2}$$

The Jaumann stress rate and Jaumann couple stress rate therein are defined by

$$\overset{0}{\sigma}_{ij} = \dot{\sigma}_{ij} - w_{ik}\sigma_{kj} + \sigma_{ik}w_{kj} \tag{3}$$

and

$$\overset{0}{m}_i = \dot{m}_i - 0.5 w_{ik} m_k + 0.5 m_k w_{ki}. \tag{4}$$

The functions $F_{ij}$ and $G_i$ in Eqs. (1) and (2) represent isotropic tensor-valued functions of their arguments; $\sigma_{ij}$ is the Cauchy stress tensor, $m_i$ is the couple stress vector, $e$ denotes the current void ratio, $d^c_{kl}$ is the polar strain rate and $k_i$ denotes the rate of curvature vector:

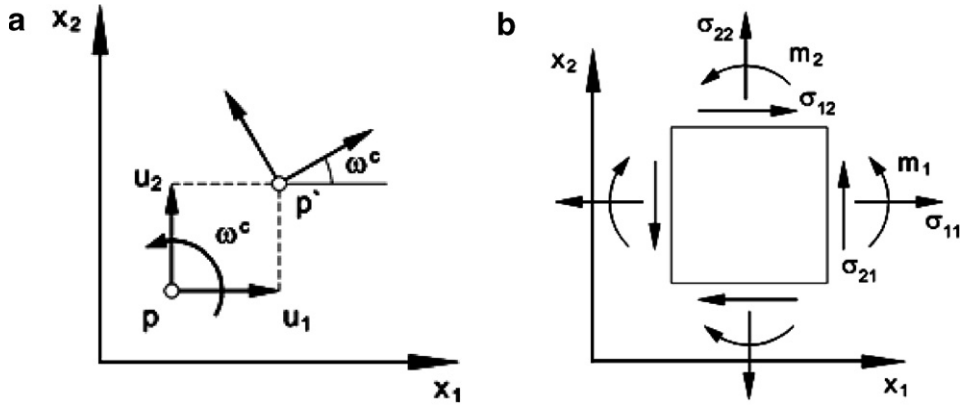


Fig. 1. Plane Cosserat continuum: (a) degrees of freedom ($u_1$, horizontal displacement; $u_2$, vertical displacement; $\omega^c$, Cosserat rotation), (b) stresses $\sigma_{ij}$ and couple stresses $m_i$ at an element.

$$d^c_{ij} = d_{ij} + w_{ij} - w^c_{ij}, \quad \text{and} \quad k_i = w^c_{,i}. \tag{5}$$

The rate of deformation tensor $d_{ij}$ and the spin tensor $w_{ij}$ are related to the velocity $v_i$ as follows:

$$d_{ij} = (v_{i,j} + v_{j,i})/2, \quad w_{ij} = (v_{i,j} - v_{j,i})/2, \quad ()_{,i} = \partial()/\partial x_i. \tag{6}$$

The rate of Cosserat rotation $w^c$ is defined by

$$w^c_{21} = -w^c_{12} = w^c \quad \text{and} \quad w^c_{kk} = 0. \tag{7}$$

For moderate pressures, the grains can be assumed to be isochoric. In this case, the change of void ratio depends only on the strain rate via

$$\dot{e} = (1+e)d_{kk}. \tag{8}$$

For the numerical calculations, the following micro-polar hypoplastic constitutive equation are employed (Tejchman and Gudehus, 2001):

$$\overset{0}{\sigma}_{ij} = f_s \left[ L_{ij}(\hat{\sigma}_{kl}, \hat{m}_k, d^c_{kl}, k_k d_{50}) + f_d N_{ij}(\hat{\sigma}_{ij}) \sqrt{d^c_{kl} d^c_{kl} + k_k k_k d^2_{50}} \right] \tag{9}$$

and

$$\overset{0}{m}_i / d_{50} = f_s \left[ L^c_i(\hat{\sigma}_{kl}, \hat{m}_k, d^c_{kl}, k_k d_{50}) + f_d N^c_i(\hat{m}_i) \sqrt{d^c_{kl} d^c_{kl} + k_k k_k d^2_{50}} \right], \tag{10}$$

wherein the normalized stress tensor $\hat{\sigma}_{ij}$ is defined by

$$\hat{\sigma}_{ij} = \frac{\sigma_{ij}}{\sigma_{kk}} \tag{11}$$

and the normalized couple stress vector $\hat{m}_i$ is defined by

$$\hat{m}_i = \frac{m_i}{\sigma_{kk} d_{50}}, \tag{12}$$

wherein $d_{50}$ is the mean grain diameter. The scalar factors $f_s = f_s(e, \sigma_{kk})$ and $f_d = f_d(e, \sigma_{kk})$ in Eqs. (9) and (10) describe the influence of density and stress level on the incremental stiffness. The factor $f_s$ depends on the granulate hardness $h_s$, the mean stress $\sigma_{kk}$, the maximum void ratio $e_i$ and the current void ratio $e$ by:

$$f_s = \frac{h_s}{n h_i} \left( \frac{1+e_i}{e_i} \right) \left( \frac{e_i}{e} \right)^{\beta} \left( -\frac{\sigma_{kk}}{h_s} \right)^{1-n} \tag{13}$$

with

$$h_i = \frac{1}{c_1^2} + \frac{1}{3} - \left( \frac{e_{i0} - e_{d0}}{e_{c0} - e_{d0}} \right)^{\alpha} \frac{1}{c_1 \sqrt{3}}. \tag{14}$$

In the above equations, the granulate hardness $h_s$ represents a reference pressure, the coefficients $\alpha$ and $\beta$ express the dependence on density and pressure respectively, and $n$ denotes the compression coefficient. The multiplier $f_d$ represents the dependence on a relative void ratio via:

$$f_d = \left( \frac{e - e_d}{e_c - e_d} \right)^{\alpha}. \tag{15}$$

The relative void ratio in the above expression involves the void ratio in critical state $e_c$, the minimum void ratio $e_d$ (the densest packing) and the maximum void ratio $e_i$ (the loosest packing). In a critical state, a granular material experiences continuous deformation while the void ratio remains unchanged. The current void ratio $e$ is bounded by the two extreme void ratios $e_i$ and $e_d$. Based on experimental observations, the void ratios $e_i$, $e_d$ and $e_c$ are assumed to depend on the pressure $\sigma_{kk}$ (Fig. 2):

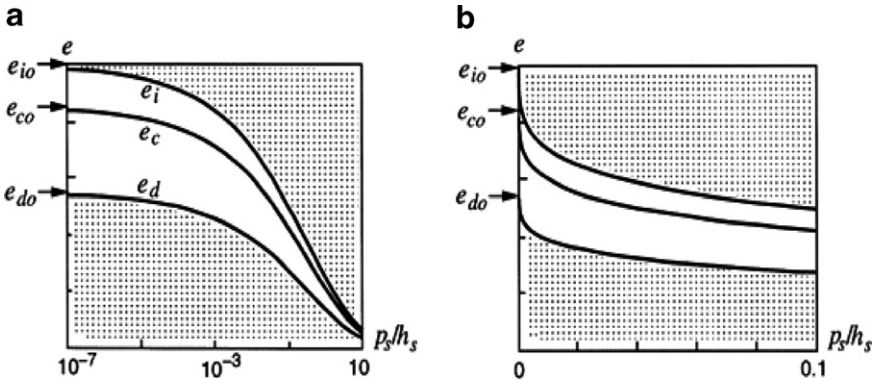


Fig. 2. Relationship between void ratios $e_i$, $e_c$ and $e_d$ and mean pressure $p_s$ in a logarithmic (a) and linear (b) scale (grey zones denote inadmissible states).

$$e_i = e_{i0}\exp[-(-\sigma_{kk}/h_s)^n], \tag{16}$$

$$e_d = e_{d0}\exp[-(-\sigma_{kk}/h_s)^n], \tag{17}$$

$$e_c = e_{c0}\exp[-(-\sigma_{kk}/h_s)^n], \tag{18}$$

wherein $e_{i0}$, $e_{d0}$ and $e_{c0}$ are the values of $e_i$, $e_d$ and $e_c$ at $\sigma_{kk} = 0$, respectively. For the functions $L_{ij}$, $N_{ij}$, $L_i^c$ and $N_i^c$, the following specific expressions are used (Tejchman and Gudehus, 2001):

$$L_{ij} = a_1^2 d_{ij}^c + \hat{\sigma}_{ij}(\hat{\sigma}_{kl} d_{kl}^c + \hat{m}_k k_k d_{50}), \tag{19}$$

$$L_i^c = a_1^2 k_i d_{50} + a_1^2 \hat{m}_i(\hat{\sigma}_{kl} d_{kl}^c + \hat{m}_k k_k d_{50}), \tag{20}$$

$$N_{ij} = a_1(\hat{\sigma}_{ij} + \hat{\sigma}_{ij}^*), \tag{21}$$

$$N_i^c = a_1^2 a_c \hat{m}_i, \tag{22}$$

where

$$a_1^{-1} = c_1 + c_2\sqrt{\hat{\sigma}_{kl}^*\hat{\sigma}_{lk}^*}[1 + \cos(3\theta)], \tag{23}$$

$$\cos(3\theta) = -\frac{\sqrt{6}}{[\hat{\sigma}_{pq}^*\hat{\sigma}_{pq}^*]^{1.5}}(\hat{\sigma}_{kl}^*\hat{\sigma}_{lm}^*\hat{\sigma}_{mk}^*) \tag{24}$$

with

$$c_1 = \sqrt{\frac{3}{8}}\frac{(3 - \sin\phi_c)}{\sin\phi_c}, \quad c_2 = \frac{3}{8}\frac{(3 + \sin\phi_c)}{\sin\phi_c}. \tag{25}$$

The parameter $\phi_c$ is the friction angle in critical states, and the parameter $\theta$ denotes the Lode angle in the deviatoric plane at $\hat{\sigma}_{ii} = 1$, and $\hat{\sigma}_{ij}^*$ denotes the deviatoric part of $\hat{\sigma}_{ij}$. The micro-polar parameter $a_c$ in Eq. (22) can be correlated with the grain roughness. This correlation can be established by studying the shearing of a narrow granular strip between two rough boundaries (Tejchman and Gudehus, 2001). It can be represented by a constant, e.g. $a_c = 1$–5, or connected to the parameter $a_1^{-1}$, e.g. $a_c = (0.5 - 1.5) \times a_1^{-1}$. The parameter $a_1^{-1}$ lies in the range of 3.0–4.3 for the usually critical friction angle.

The constitutive relationship requires the following ten material parameters: $e_{i0}$, $e_{d0}$, $e_{c0}$, $\phi_c$, $h_s$, $\beta$, $n$, $\alpha$, $a_c$ and $d_{50}$. The parameters $h_s$ and $n$ are estimated from a single oedometric compression test with an initially loose specimen ($h_s$ reflects the slope of the curve in a semi-logarithmic representation, and $n$ its curvature). The parameters $\alpha$ and $\beta$ can be determined from a triaxial or plane strain test with a dense specimen and trigger the magnitude and position of the peak friction angle. The critical friction angle $\phi_c$ can be determined from the angle of repose or measured in a triaxial test with a loose specimen. The parameters $e_{i0}$, $e_{d0}$, $e_{c0}$ and $d_{50}$ are obtained from conventional index tests ($e_{c0} \approx e_{\max}$, $e_{d0} \approx e_{\min}$, $e_{i0} \approx (1.1\text{–}1.5)e_{\max}$). A calibration procedure was given in detail by Herle and Gudehus (1999).

## 3. FE-input data

### 3.1. Deterministic calculations

The FE-calculations of a plane strain compression test (assuming a uniform distribution of the initial void ratio $e_0$) were performed with six different sand specimen sizes $b_0 \times h_0$ ($b_0$, initial width; $h_0$, initial height) which were geometrically similar: $10 \times 35$, $20 \times 70$, $40 \times 140$, $80 \times 280$, $160 \times 560$ and $320 \times 1120$ mm$^2$ (Tejchman and Górski, 2007b). The specimen depth was equal to $l = 1.0$ m with plane strain condition. The specimen dimensions of $40 \times 140$ mm$^2$ were similar as in the experiments by Vardoulakis (1977) and Vardoulakis et al. (1978). In all cases, 896 quadrilateral elements divided into 3584 triangular elements were used. The quadrilateral elements composed of four diagonally crossed triangles were used to avoid volumetric locking due to dilatancy effects (Groen, 1997). Linear shape functions were used for displacements and for the Cosserat rotation. The integration was performed with one sampling point placed in the middle of each element. To properly capture shear localization inside of the granular specimen, the size of the finite elements $s_e$ should be not larger than five mean grain diameters $d_{50}$ (Tejchman and Bauer, 1996). For specimen sizes changing from $10 \times 35$ up to $40 \times 140$ mm$^2$ this condition was fulfilled ($s_e \leqslant 5 \times d_{50}$). However, for specimen sizes larger than $40 \times 140$ mm$^2$ this condition was violated (e.g $s_e = 40 \times d_{50}$ for $320 \times 1120$ mm$^2$). Thus, these latter FE-results were mesh-dependent; the mesh-dependence increased with increasing specimen size. A further increase of the amount of finite elements would increase the computation time drastically. A remedy in the form of remeshing (which is effective in such cases, Ehlers and Graf, 2003) was not the aim of our FE-analyses.

A quasi-static deformation in sand was imposed through a constant vertical displacement increment $\Delta u$ prescribed at nodes along the upper edge of the specimen. The boundary conditions implied no shear stress imposed at the smooth top and bottom of the specimen. To preserve the stability of the specimen against horizontal sliding, the node in the middle of the top edge was kept fixed. To simulate a movable roller bearing in the experiment (Vardoulakis et al., 1978), the horizontal displacements along the specimen bottom were constrained to move by the same amount. Thus, no imperfections were used to induce shear localization with an uniform distribution of $e_0$. Comparative calculations were also performed with a very rough top and bottom boundary. In this case, the horizontal displacement and Cosserat rotation along both horizontal edges were assumed to be equal to zero. The vertical displacement increments were chosen as $\Delta u/h_0 = 0.0000025$. About 3000 steps were performed.

As an initial stress state, a $K_0$-state with $\sigma_{22} = \gamma_d x_2$ and $\sigma_{11} = K_0 \gamma_d x_2$ was assumed in the specimen; $x_2$ is the vertical coordinate measured from the top of the specimen, $\gamma_d = 16.5$ kN/m$^3$ denotes the initial volumetric weight and $K_0 = 0.50$ is the earth pressure coefficient at rest ($\sigma_{11}$, horizontal normal stress; $\sigma_{22}$, vertical normal stress). Then, a uniform confining pressure of $\sigma_c = 200$ kPa was prescribed.

For the solution of a non-linear equation system, a modified Newton–Raphson scheme with line search was used. The global stiffness matrix was calculated with only line terms of the constitutive equations (Eqs. (1) and (2)). The stiffness matrix was updated every 100 steps. In order to accelerate the convergence in the softening regime, the initial increments of displacements and Cosserat rotations in each calculation step were assumed to be equal to the final increments in the previous step. The procedure was found to yield sufficiently accurate solutions with a fast convergence. The magnitude of the maximum out-of-balance force at the end of each calculation step was found to be smaller than 2% of the calculated total vertical force of the granular specimen. Due to non-linear terms in deformation rate and material softening this procedure turned out to be more efficient than a full Newton–Raphson method. The iteration steps were performed using translational and rotational convergence criteria. For the time integration of stresses in finite elements, a one-step Euler forward scheme was applied. The calculations were carried out with large deformations and curvatures using a so-called "Updated Lagrangian" formulation by taking into account the Jaumann stress rate and Jaumann couple stress rate and the actual shape and area of finite elements.

### 3.2. Statistical calculations

In the case of nonlinear random field calculations, the only reliable solution is the direct Monte Carlo method. Contrary to stochastic finite element codes, the Monte Carlo method does not impose any restriction

to the solved random problems. The only limitation of the Monte Carlo method is the time of calculations. To reproduce exactly the input random data at least 2000 random samples should be used (Bielewicz and Górski, 2002; Górski, 2006). Any nonlinear calculations for such number of initial data are, however, impossible due too excessive computation times. To determine a minimal, but sufficient number of samples (which allows to estimate the results with a specified accuracy), a convergence analysis of the outcomes has been proposed (Bielewicz and Górski, 2002). It has been estimated that in case of various engineering problems only ca. 50 realizations have to be considered. A further decrease of sample numbers can be obtained using Monte Carlo reduction methods. In the paper by Tejchman and Górski (2007a) stratified and Latin sampling methods were considered. It should be pointed out that these methods were not used for the generation of two-dimensional random fields, but for their classification. The calculations have shown that using these reduction methods the results can be properly estimated by several realizations (e.g. 12–15). Following this conclusion, in this work the Latin sampling method was applied.

According to the Latin hypercube sampling method, the random field realizations were chosen in a strictly defined manner (Fig. 3). First, an initial set of random samples was generated in the same way as in the case of the direct Monte Carlo method. Next, the generated samples were classified according to chosen parameters, for example norms of the random vectors, mean values, changes of the vector signs and others. The samples were arranged according to this classification. On this basis, their distributions in the form of frequency histograms were specified. The whole space of the samples was divided into subsets of equal probability and numbered. The Latin hypercube sampling method combines at random each subset number with other subset numbers of the remaining variables only once. From each subset defined in this way, only one sample was chosen for the analysis (Fig. 3).

The input data of the considered problem was a set of random fields describing the initial void ratio $e_0$. A truncated Gaussian random field was applied

$$e_0 = \bar{e}_0(1 + v\beta(x_1, x_2)), \tag{26}$$

where $\bar{e}_0$ is the mean value of the initial void ratio, $v = s_{e_0}/\bar{e}_0$ is the coefficient of variation, $s_{e_0}$ describes the standard deviation of the mean value, and $\beta(x_1, x_2)$ stands for the normalized homogeneous random field. Randomness of the initial void ratio was described by a correlation function. For lack of the appropriate data the correlation function is usually chosen arbitrarily. Here, the following second order, homogeneous correlation function was adopted (Bielewicz and Górski, 2002)

$$K(x_1, x_2) = s_{e_0}^2 \times \mathrm{e}^{-\lambda_{x_1}\Delta x_1}(1 + \lambda_{x_1}\Delta x_1)\mathrm{e}^{-\lambda_{x_2}\Delta x_2}(1 + \lambda_{x_2}\Delta x_2), \tag{27}$$

where $\Delta x_1$ and $\Delta x_2$ is are the distances between two field points along the horizontal axis $x_1$ and vertical axis $x_2$, $\lambda_{x1}$ and $\lambda_{x2}$ are the decay coefficients (damping parameters) characterizing a spatial variability of the specimen properties (i.e. describe the correlation between the random field points), while the standard deviation $s_{e_0}$ represents the field scattering. The scale of fluctuation $\theta$ (introduced by Vanmarcke, 1983) to approximate the variance function by a parameter independently of the character and shape of the correlation function was

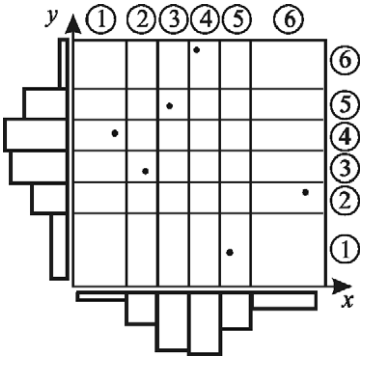


Fig. 3. Latin hypercube method – the scheme of random sampling.

$\theta = 4/\lambda$ (for the normalized function of Eq. (27) with $\Delta x \to 0$). The parameter is twice as big as the fluctuation scale of a standard first order correlation function $K(x_1, x_2) = \mathrm{e}^{-\lambda_{x_1}\Delta x_1}\mathrm{e}^{-\lambda_{x2}\Delta x_2}$ (Knabe et al., 1998). Thus, by using appropriate values of the decay coefficients $\lambda$, the second order correlation function can be approximated by the first order one. It was demonstrated that the results obtained using these two functions described by the same scale of fluctuation are almost identical (Przewłócki and Górski, 1999). The second order homogeneous function (Eq. (27)) proved to be very useful (Przewłócki and Górski, 2001).

In finite element methods, continuous functions are represented by a finite set of nodal point parameters. The same has to be applied to random fields. A discretization procedure is the approximation of a random field by its estimator defined by means of a finite set of random variables grouped in a random vector. The discretization methods can be divided into the following groups: point discretization methods, average discretization methods and series expansion methods. Here, the procedure of local averages of the random fields proposed by Vanmarcke (1983) was adopted. After an appropriate integration of the correlation function (Eq. (27)), the following expression describing the variances $D_w$ and covariances $K_w$ were obtained (Knabe et al., 1998):

$$D_w(\Delta x_1, \Delta x_2) = \frac{2}{\lambda_{x_1}\Delta x_1} s_{e_0}^2 \left[2 + \mathrm{e}^{-\lambda_{x_1}\Delta x_1} - \frac{3}{\lambda_{x_1}\Delta x_1}(1 - \mathrm{e}^{-\lambda_{x_1}\Delta x_1})\right] \times \frac{2}{\lambda_{x_2}\Delta x_2}\left[2 + \mathrm{e}^{-\lambda_{x_2}\Delta x_2} - \frac{3}{\lambda_{x_2}\Delta x_2}\left(1 - \mathrm{e}^{-\lambda_{x_2}\Delta x_2}\right)\right], \tag{28}$$

$$K_w(\Delta x_1, \Delta x_2) = \frac{\mathrm{e}^{\lambda_{x_1}\Delta x_1}}{(\lambda_{x_1}\Delta x_1)^2} s_{e_0}^2 \left\{[\cos(\lambda_{x_1}\Delta x_1) - \sin(\lambda_{x_1}\Delta x_1)] + 2\lambda_{x_1}\Delta x_1 - 1\right\} \times \frac{\mathrm{e}^{\lambda_{x_2}\Delta x_2}}{(\lambda_{x_2}\Delta x_2)^2} s\left\{[\cos(\lambda_{x_2}\Delta x_2) - \sin(\lambda_{x_2}\Delta x_2)] + 2\lambda_{x_2}\Delta x_2 - 1\right\}. \tag{29}$$

The random fields were generated using a conditional rejection method proposed by Walukiewicz et al. (1997). According to his method a discrete random field was described by multidimensional random variables defined at mesh nodes. The random variable vector of initial void ratio $\mathbf{e}_0(m \times 1)$ was divided into blocks consisting of the unknown $\mathbf{e}_{ou}(n \times 1)$ and the known $\mathbf{e}_{ok}(p \times 1)$ elements $(n + p = m)$. The covariance matrix $\mathbf{K}(m \times m)$ and the expected values vector $\bar{\mathbf{e}}_0(m \times 1)$ were also appropriately split:

$$\mathbf{e}_0 = \begin{Bmatrix} \mathbf{e}_{ou} \\ \mathbf{e}_{ok} \end{Bmatrix} \begin{matrix} n \\ p \end{matrix}, \quad \mathbf{K} = \begin{bmatrix} \mathbf{K}_{11} & \mathbf{K}_{12} \\ \mathbf{K}_{21} & \mathbf{K}_{22} \end{bmatrix} \begin{matrix} n \\ p \end{matrix}, \quad \bar{\mathbf{e}}_0 = \begin{Bmatrix} \bar{\mathbf{e}}_{ou} \\ \bar{\mathbf{e}}_{ok} \end{Bmatrix} \begin{matrix} n \\ p \end{matrix}. \tag{30}$$

$$\begin{matrix} n & p \end{matrix}$$

The unknown vector $\mathbf{e}_{ou}$ was estimated from the following conditional truncated distribution

$$f_t(\mathbf{e}_{ou}/\mathbf{e}_{ok}) = (1-t)^{-m/2}(\det \mathbf{K}_c)^{-1/2}(2\pi)^{-m/2} \times \exp\left(-\frac{1}{2(1-t)}(\mathbf{e}_{ou} - \bar{\mathbf{e}}_{oc})^{\mathrm{T}}\mathbf{K}_c^{-1}(\mathbf{e}_{ou} - \bar{\mathbf{e}}_{oc})\right), \tag{31}$$

where $\mathbf{K}_c$ and $\bar{\mathbf{e}}_{oc}$ are described as the conditional covariance matrix and conditional expected value vector:

$$\mathbf{K}_c = \mathbf{K}_{11} - \mathbf{K}_{12}\mathbf{K}_{22}^{-1}\mathbf{K}_{21}, \tag{32}$$

$$\bar{\mathbf{e}}_{oc} = \bar{\mathbf{x}}_u + \mathbf{K}_{12}\mathbf{K}_{22}^{-1}(\mathbf{e}_{ok} - \bar{\mathbf{e}}_{ok}). \tag{33}$$

The constant $t$ in Eq. (31) is the truncation parameter

$$t = \frac{s_{e_0} \cdot \exp(-s_{e_0}^2/2)}{\sqrt{2\pi} erf(s_{e_0})} \tag{34}$$

with

$$erf(s_{e_0}) = \frac{1}{\sqrt{2\pi}} \int_0^{s_{e_0}} \exp\left(-\frac{x^2}{2}\right) dx. \tag{35}$$

According to the conditional rejection method, any mesh point value is generated using the values calculated earlier. When large problems are solved, such approach is inefficient. Therefore, a kind of 'base scheme' was defined (Walukiewicz et al., 1997). The scheme covered a limited mesh area (hundred points), and only these points were used in the calculations of the next random values (Fig. 4). The simulation process was divided into three stages. First, the four-corner random values were generated (Fig. 4a) using an unconditional method. Next, all random variables in the defined base scheme (dotted rectangle in Fig. 4) were generated, one by one, using the conditional method (Fig. 4b). In the third stage, the base scheme was appropriately shifted, and the next group of unknown random values was simulated (Fig. 4c). The base scheme was translated so as to cover all the field nodes (Fig. 4d). It is noted that this approach allows for generation of practically unlimited random fields (thousands of discrete points).

To describe the discrepancies between the theoretical (Eqs. (28) and (29)) and generated fields, the following global $G_{er}$ and local $V_{er}$ errors were calculated (Walukiewicz et al., 1997):

$$G_{er}(\mathbf{K},\widehat{\mathbf{K}}) = \frac{|\|\mathbf{K}\| - \|\widehat{\mathbf{K}}\||}{\|\mathbf{K}\|} \times 100\%, \tag{36}$$

$$V_{er}(k_{ii},\hat{k}_{ii}) = \sum_{i=1}^{m} \frac{(k_{ii} - \hat{k}_{ii})}{(k_{ii})} \times 100\%, \tag{37}$$

where $\widehat{\mathbf{K}}$ is the estimator of the covariance matrix $\mathbf{K}$

$$\widehat{\mathbf{K}} = \frac{1}{NR-1}\sum_{i=1}^{NR}(\hat{\mathbf{e}}_{oi} - \bar{\hat{\mathbf{e}}}_0)(\hat{\mathbf{e}}_{oi} - \bar{\hat{\mathbf{e}}}_0)^{\mathrm{T}}, \quad \bar{\hat{\mathbf{e}}}_0 = \frac{1}{NR}\sum_{i=1}^{NR}\hat{\mathbf{e}}_{oi}. \tag{38}$$

The parameter $\hat{\mathbf{e}}_0$ is the estimator of the random vector $\mathbf{e}_0$, and $\bar{\hat{\mathbf{e}}}_0$ is the estimator of its mean value, $NR$ denotes the number of realizations, $\|\mathbf{K}\| = \sqrt{\mathrm{tr}(\mathbf{K})^2}$ is the matrix norm, $k_{ii}$ and $\hat{k}_{ii}$ denote the diagonal element of the covariance matrix $\mathbf{K}$ and its estimators $\widehat{\mathbf{K}}$, respectively.

When a stochastic distribution of the initial void ratio was assumed, two different specimen sizes were used: $40 \times 140\ \mathrm{mm}^2$ (medium size) and $320 \times 1120\ \mathrm{mm}^2$ (large size). In the probabilistic calculations, the same

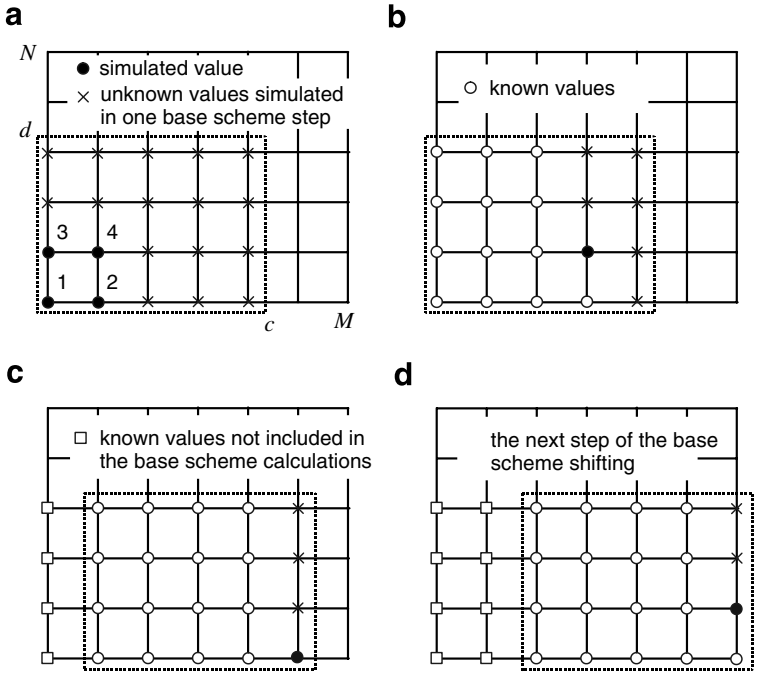


Fig. 4. Successive coverage of the field points with the moving propagation scheme (Walukiewicz et al., 1997).

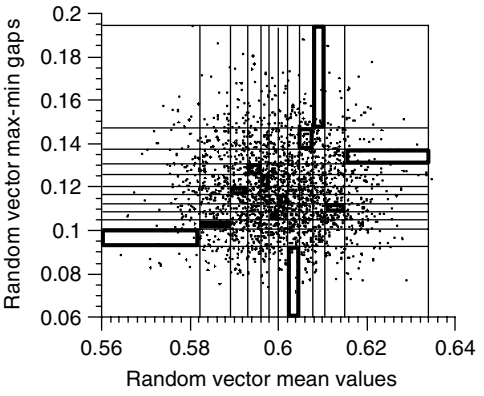


Fig. 5. Selection of 12 pairs of random samples using Latin hypercube sampling: 1–2, 2–3, 3–7, 4–9, 5–8, 6–4, 7–6, 8–1, 9–11, 10–12, 11–5 and 12–10.

assumption as in the case of a deterministic analysis were applied: a mean value of the initial void ratio $\bar{e}_0 = 0.60$ (initially dense sand). First, we assumed a strong correlation of the initial void ratio $e_0$ in both directions ($\lambda_{x1} = 1$ and $\lambda_{x2} = 1$ in Eqs. (28) and (29)) and a low standard deviation $s_d = 0.05$ to simulate a careful specimen preparation method (Vardoulakis et al., 1978). In this case, the range of significant correlation was approximately 60 mm. In addition, the calculations were performed for a weak correlation of $e_0$ in both directions ($\lambda_{x1} = 3$ and $\lambda_{x2} = 3$ in Eqs. (28) and (29)) and a large standard deviation $s_d = 0.10$ (the correlation range was about 40 mm). The initial void ratio scattering in the specimen was also limited by the pressure dependent void ratios $e_{i0}$ (upper bound) and $e_{d0}$ (lower bound) (Eqs. (16) and (17)). The truncation parameter $t$ of the Gaussian field (Eq. (34)) allows to fulfill these conditions. The dimension of the random field was the same as the finite element mesh, i.e. $m = 16 \times 56 = 896$ points. The following dimension of the base scheme was applied: $c = d = 16$ (Fig. 4). Using the algorithm described above, 2000 field realizations of the initial void ratio were generated. The global $G_{er}$ and local (variance) $V_{er}$ errors of the generation were calculated (Eqs. (36) and (37)): $G_{er} = 2.02$, $V_{er} = 1.44$. Next, the generated fields were classified according to two parameters: the mean value of the initial void ratio and the gap between the lowest and the highest value of the initial void ratio. The joint probability distribution (so-called ''ant hill'') is presented in Fig. 5. One dot represents one random vector described by its mean value and the difference between its extreme values. The two variable domains were divided in 12 intervals of equal probabilities (see vertical and horizontal lines in Fig. 5). Next, according to the Latin hypercube sampling assumptions, 12 random numbers in the range 1–12 were generated (one number appeared only once) using the uniform distribution. The generated numbers formed the following 12 pairs: 1–2, 2–3, 3–7, 4–9, 5–8, 6–4, 7–6, 8–1, 9–11, 10–12, 11–5 and 12–10. According to these pairs, the appropriate areas (subfields) were selected (they are presented as rectangles in Fig. 5). From each subfield only one realization was chosen and used as the input data to the FEM calculations. In this way the results of 12 realizations were analyzed.

## 4. FE-results

### 4.1. Deterministic size effect

#### 4.1.1. Smooth boundaries

Fig. 6 shows results for an initially dense sand during plane strain compression for six different specimen sizes $b_0 \times h_0$ (same $b_0/h_0$): $10 \times 35$, $20 \times 70$, $40 \times 140$, $80 \times 280$, $160 \times 560$ and $320 \times 1112$ mm$^2$, with a uniform distribution of the initial void ratio $e_0 = 0.60$ and the lateral confining pressure $p = 200$ kPa. Presented is the evolution of the normalized vertical force $P/(\sigma_c b_0 l)$ versus the normalized vertical displacement of the top boundary $u_2^t/h_0$ (Tejchman and Górski, 2007b). In addition, the deformed FE-meshes for

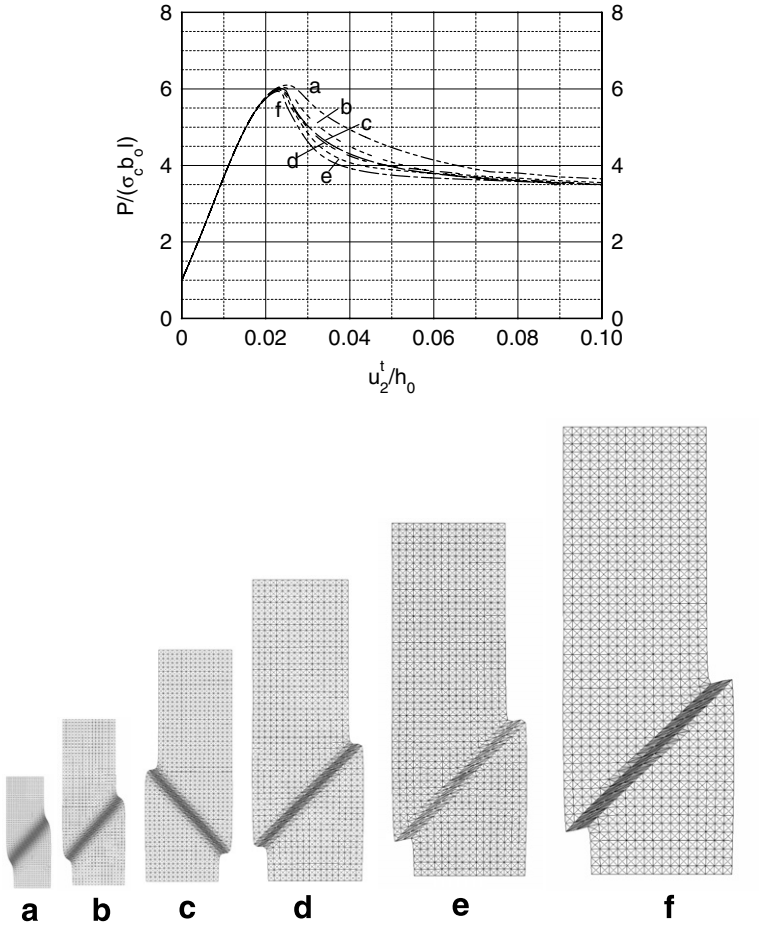


Fig. 6. Evolution of normalized vertical force $P/(\sigma_c b_0 l)$ versus normalized vertical displacement of the upper edge $u_2^t/h_0$ and deformed FE-meshes with the distribution equivalent total strain measure during plane strain compression with a dense specimen ($e_0 = 0.60$) for six different specimen sizes: (a) $10 \times 35$ mm$^2$, (b) $20 \times 70$ mm$^2$, (c) $40 \times 140$ mm$^2$, (d) $80 \times 280$ mm$^2$, (e) $160 \times 560$ mm$^2$, (f) $320 \times 1120$ mm$^2$ (uniform distribution of initial void ratio, smooth edges) (note that the specimens are not proportionally scaled).

different sizes at $u_2^t/h_0 = 0.075$ with the distribution of the distribution of equivalent total strain $\bar{\varepsilon} = \sqrt{\varepsilon_{ij}\varepsilon_{ij}}$ are additionally shown in Fig. 6 (Tejchman and Górski, 2007b). Table 1 presents overall internal friction angles at peak $\phi^p$ and residual friction angles $\phi_{cr}$ (at $u_2^t/h_0 = 0.10$), vertical strain corresponding to the maximum force $u_2^t/h_0$ and normalized shear zone thickness $t_s/d_{50}$ (Tejchman and Górski, 2007b). The overall friction angle was calculated from the formula including the principal stresses on the basis of the Mohr's circle

$$\phi = \arcsin\left|\frac{\sigma_1 - \sigma_2}{\sigma_1 + \sigma_2}\right| \tag{39}$$

with $\sigma_1 = P/(bl)$($b$ is the actual specimen width) and $\sigma_2 = \sigma_c$ ($\sigma_c = 200$ kPa – uniform confining pressure).

The resultant vertical force on the specimen top increases first, shows a pronounced peak, drops later and reaches then a residual value. The strength increases and the softening rate decreases with decreasing specimen size. The peak friction angle $\phi_p$ insignificantly increases, only from $\phi_p = 45.38°$ ($32 \times 1120$ mm$^2$) to $\phi_p = 45.92°$ ($10 \times 35$ mm$^2$), due to a similar failure mechanism and pressure level. The vertical strain corresponding to the peak grows with decreasing specimen size (from 2.29% up to 2.50%). The residual friction angle is similar for all specimen sizes, it changes between 34.5° and 36° at $u_2^t/h_0 = 7.5\%$.

Table 1
The values of peak friction angles $\phi^p$, residual friction angles $\phi_{cr}$, vertical strain corresponding to the maximum vertical force $u_2^t/h_0$, normalized shear zone thickness $t_s/d_{50}$ (uniform distribution of initial void ratio with $e_0 = 0.60$, smooth boundaries)

| Specimen size $b_0 \times h_0$ (mm$^2$) | $\phi^p$ [°] | $\phi_{cr}$ [°] | $U_2^t/h_0$ | $t_s/d_{50}$ |
|---|---|---|---|---|
| $10 \times 35$ | 45.92 | 35.9 | 0.0250 | 7 |
| $20 \times 70$ | 45.71 | 34.7 | 0.0240 | 11 |
| $40 \times 140$ | 45.62 | 34.8 | 0.0236 | 14 |
| $80 \times 280$ | 45.55 | 35.4 | 0.0233 | 28 |
| $160 \times 560$ | 45.48 | 35.20 | 0.0231 | 46 |
| $320 \times 1120$ | 45.38 | 34.5 | 0.0229 | 46 |

The obtained friction angles at peak and at residual state, and the corresponding vertical shortening of the sand specimen for the specimen of $40 \times 140$ mm$^2$ ($\phi^p = 45.6°$, $\phi_{\text{res}} = 34°$, $u_2^t/h_0 = 0.0236$) are in a satisfactory agreement with laboratory results with Karlsruhe sand carried out by Vardoulakis (1977) and Vardoulakis et al. (1978), where the dimensions of the sand specimen were: $h_0 = 140$ mm, $b_0 = 40$ mm and $l_0 = 80$ mm.

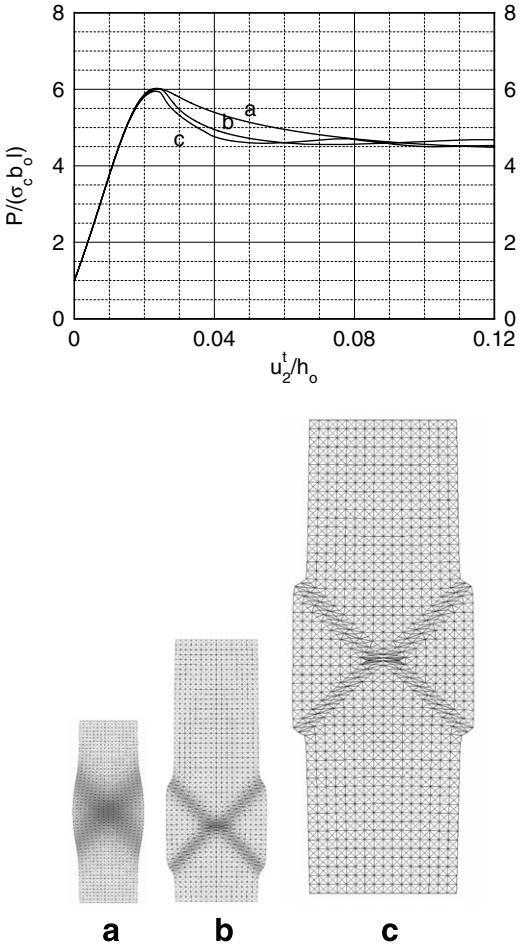


Fig. 7. Evolution of normalized vertical force $P/(\sigma_c b_0 l)$ versus normalized vertical displacement of the upper edge $u_2^t/h_0$ and deformed FE-meshes with the distribution equivalent total strain measure during plane strain compression with a dense specimen ($e_0 = 0.60$) for three different specimen sizes: (a) $10 \times 35$ mm$^2$; (b) $40 \times 140$ mm$^2$; (c) $320 \times 1120$ mm$^2$ (uniform distribution of initial void ratio, very rough boundaries) (note that the specimens are not proportionally scaled).

The experiments with dense sand ($e_0 = 0.55$–$0.60$) resulted in $\phi_p = 45$–$48°$ and $\phi_{cr} = 32$–$33°$ at $\sigma_c = 200$ kPa. However, the calculated stiffness is higher before the peak than observed.

The thickness of the shear zone at mid-point of the specimen increases with increasing specimen size; it varies between $7 \times d_{50}$ up to $46 \times d_{50}$. The thickness of the shear zone for the specimen sizes larger than $40 \times 140$ mm$^2$ is certainly influenced by the mesh discretisation (as it was noted in Section 3.1) – it is too large. The thickness of the shear zone was determined on the basis of shear deformation and Cosserat rotation. To define the edges of the shear zone, we assumed that the Cosserat rotation larger than 0.1 occurred in the shear zone. The calculated thickness for the specimen of $40 \times 140$ mm$^2$, $t_s = 14 \times d_{50,}$ is similar as the observed thickness, $t_s = 15 \times d_{50,}$ during plane strain compression tests with dense sand ($e_0 = 0.60$) at $\sigma_c = 200$ kPa (Vardoulakis, 1977). The calculated inclination of the shear zone (about $\theta = 53$–$54°$) is also close to the experiment with dense sand (55–60°). The thickness of the shear zone on the basis of an increase of void ratio is slightly larger because each dense granulate undergoes dilatancy before shear localization occurs.

*4.1.2. Very rough boundaries*

Results for an initially dense sand during plane strain compression for three different specimen sizes $b_0 \times h_0$ (geometrically similar): $10 \times 35$, $40 \times 140$ and $320 \times 1112$ mm$^2$ with a uniform distribution of the initial void ratio $e_0 = 0.60$, lateral confining pressure of 200 kPa and very rough horizontal boundaries are shown in Fig. 7 and Table 2.

The evolution of the normalized vertical force is similar as for smooth plates. The friction angle at peak $\phi_p$ increases from: $\phi_p = 45.4°$ ($32 \times 1120$ mm$^2$) to $\phi_p = 45.7°$ ($10 \times 35$ mm$^2$) (the values are almost identical as for smooth plates). The residual friction angle changes between 39.5° and 40.4° at $u_2^t/h_0 = 10\%$. It is significantly higher (by about 5°) than for smooth plates.

In contrast to smooth plates, two symmetric intersecting shear zones always appear inside of the specimen (Fig. 7).

Table 2
The values of peak friction angles $\phi^p$, residual friction angles $\phi_{cr}$, vertical strain corresponding to the maximum vertical force $u_2^t/h_0$, normalized shear zone thickness $t_s/d_{50}$ (uniform distribution of initial void ratio with $e_0 = 0.60$, very rough boundaries)

| Specimen size $b_0 \times h_0$ (mm$^2$) | $\phi^p$ [°] | $\phi_{cr}$ [°] | $u_2^t/h_0$ | $t_s/d_{50}$ |
|---|---|---|---|---|
| $10 \times 35$ | 45.70 | 39.40 | 0.0235 | 9 |
| $40 \times 140$ | 45.60 | 40.40 | 0.0239 | 13 |
| $320 \times 1120$ | 45.40 | 39.70 | 0.0234 | 57 |

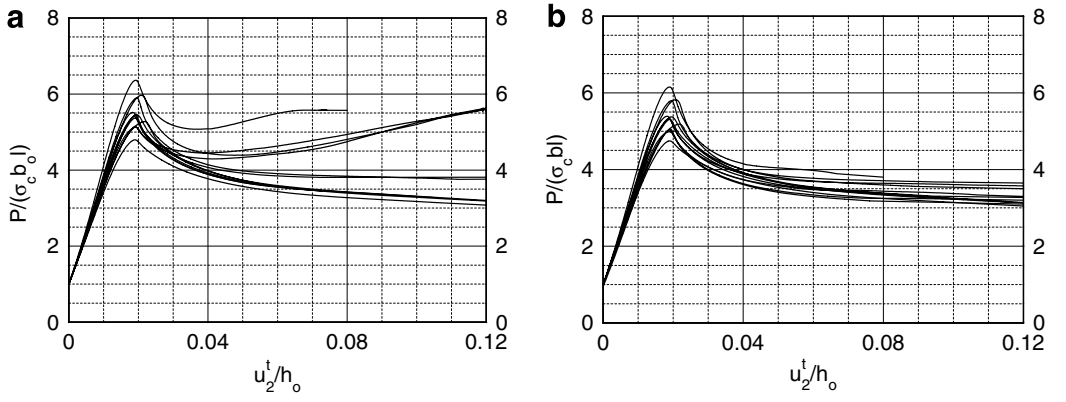


Fig. 8. Evolution of normalized vertical force $P/(\sigma_c b_0 l)$ (a) and $P/(\sigma_c b l)$ (b) versus normalized vertical displacement of the upper edge $u_2^t/h_0$ during plane strain compression with a dense specimen for 12 different random fields of $e_0$ ($\bar{e}_0 = 0.60$, specimen size $40 \times 140$ mm$^2$, smooth boundaries, $\lambda_{x1} = 1$, $\lambda_{x2} = 1$, $s_d = 0.05$).

### 4.2. Statistical size effect

#### 4.2.1. Medium sand specimen (smooth boundaries, specimen $40 \times 140$ mm$^2$, $\lambda_{x1} = 1$, $\lambda_{x2} = 1$, $s_d = 0.05$)

Twelve selected random samples using Latin hypercube sampling are shown in Fig. 5. The evolution of the normalized vertical force with respect to the initial specimen width $b_0$, $P/(\sigma_c b_0 l)$ (Fig. 8a), and with respect to the actual specimen width $b$, $P/(\sigma_c b l)$ (Fig. 8b), versus the normalized vertical displacement of the top boundary $u_2^t/h_0$ and the deformed FE-meshes at $u_2^t/h_0 = 0.075$ with the distribution of equivalent total strain $\bar{\varepsilon} = \sqrt{\varepsilon_{ij}\varepsilon_{ij}}$ are shown in Figs. 8 and 9, respectively ($b$ – actual specimen width). Table 3 includes overall friction angles at peak $\phi^p$, residual friction angle $\phi_{cr}$, vertical strain corresponding to the maximum force $u_2^t/h_0$ and normalized shear zone thickness $t_s/d_{50}$ for 12 random fields.

The evolution of the normalized vertical force depends of the location of the shear zone. If this hits the top boundary, the residual normalized vertical force $P/(\sigma_c b_0 l)$ has a increasing tendency (caused by an increase of the specimen's width). If the shear zone intersects the vertical sides the evolution of the residual normalized vertical force $P/(\sigma_c b_0 l)$ is similar as for a uniform distribution of $e_0$. The shear zone develops inside of the specimen somewhere at the weakest spot, depending on the initial distribution of $e_0$ (Fig. 8). The shear zone width changes between $11 \times d_{50}$ and $17 \times d_{50}$.

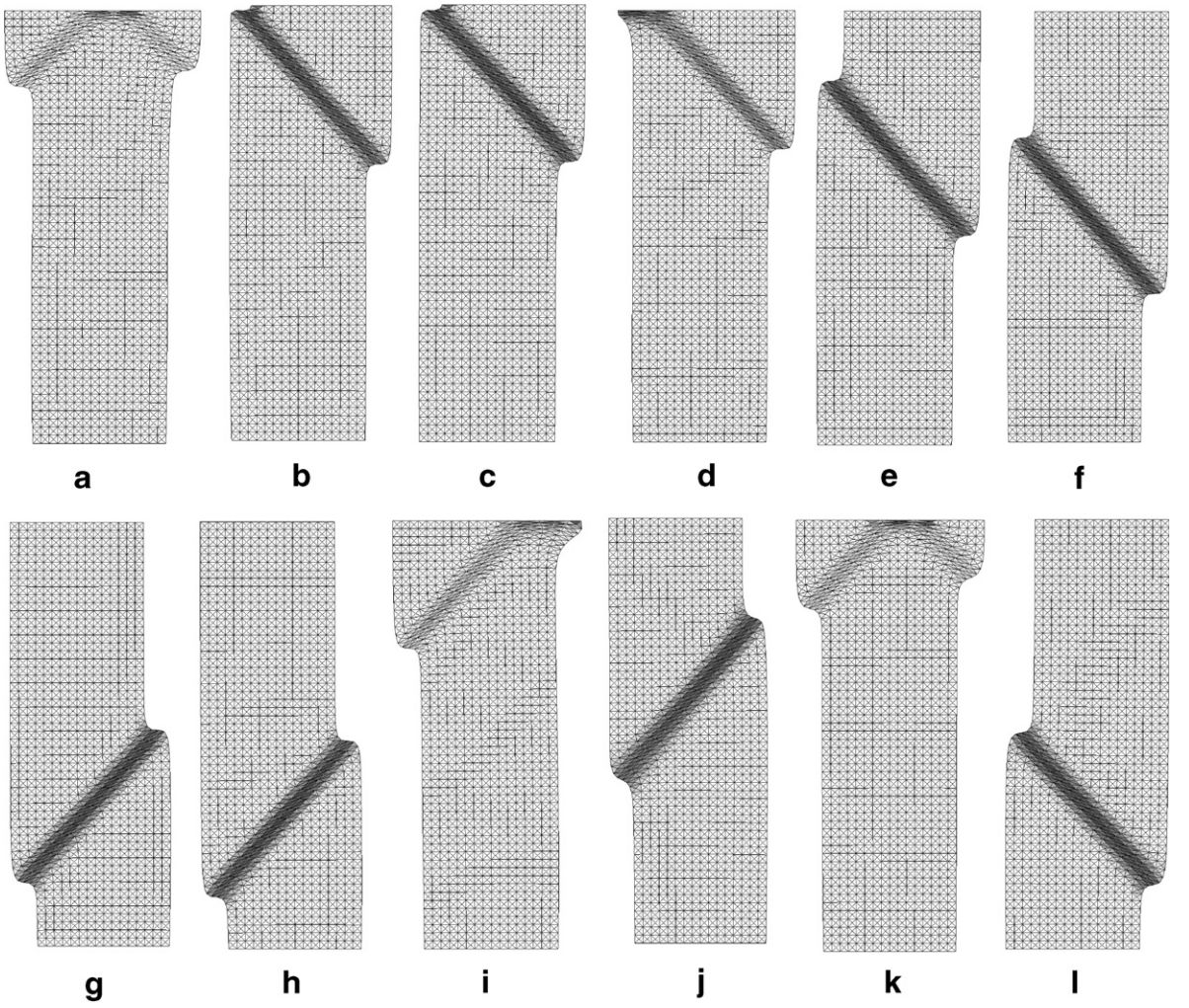


Fig. 9. Deformed FE-mesh with the distribution equivalent total strain measure during compression with a dense specimen for 12 different random fields of $e_0$ ($\bar{e}_0 = 0.60$, specimen size $40 \times 140$ mm$^2$, smooth boundaries, $\lambda_{x1} = 1$, $\lambda_{x2} = 1$, $s_d = 0.05$).

Table 3
The values of peak friction angles $\phi^p$, residual friction angles $\phi_{cr}$, vertical strain corresponding to the maximum vertical force $u_2^t/h_0$, normalized shear zone thickness $t_s/d_{50}$ for different random fields ($\bar{e}_0 = 0.60$, $b_0 = 40$ mm, $h_0 = 140$ mm, smooth boundaries, $\lambda_{x1} = 1$, $\lambda_{x2} = 1$, $s_d = 0.05$)

| Nr | $\phi^p$ [°] | $\phi_{cr}$ [°] | $u_2^t/h_0$ | $t_s/d_{50}$ |
|---|---|---|---|---|
| S-01[a] | 46.87 | 35.60 | 0.0193 | 14 |
| S-02[a] | 45.26 | 34.91 | 0.0196 | 11 |
| S-03[a] | 43.87 | 32.90 | 0.0184 | 14 |
| S-04[a] | 45.47 | 34.43 | 0.0209 | 11 |
| S-05 | 43.63 | 33.55 | 0.0196 | 14 |
| S-06 | 43.49 | 33.11 | 0.0188 | 14 |
| S-07 | 43.31 | 33.32 | 0.0187 | 14 |
| S-08 | 43.61 | 33.18 | 0.0192 | 14 |
| S-09[a] | 42.34 | 31.92 | 0.0193 | 14 |
| S-10 | 42.95 | 33.05 | 0.0218 | 17 |
| S-11[a] | 42.43 | 32.90 | 0.0190 | 17 |
| S-12 | 40.91 | 32.33 | 0.0190 | 14 |
| Mean value | 43.67 | 33.43 | 0.0195 | 14 |
| Uniform distribution of $e_0$ | 45.62 | 34.80 | 0.0236 | 14 |

[a] Shear zone hitting the top boundary.

The estimated expected value and standard deviations were for the peak friction angles $\hat{\phi}_p = 43.67°$ and $\hat{s}_{\phi_p} = 1.52$, the normalized horizontal displacement of the top boundary $u_1^t/h_0$ corresponding to the peak $\hat{u}_1^t/h_0 = 0.0195$ and $\hat{s}_{u_1^t}/h_0 = 0.00092$ and the normalized shear zone thickness $\hat{t}_s/d_{50} = 14$. and $\hat{s}_{t_s}/d_{50} = 1.7$. The peak friction angle ($\hat{\phi}_p = 43.74°$) is by 2° smaller than with a uniform initial void ratio ($\phi_p = 45.62°$), whereas the shear zone thickness is similar. The residual friction angle ($\phi_{cr} = 33.4°$ at $u_2^t/h_0 = 7.5\%$) is by 1°-2° smaller. The residual friction angle is slightly larger if the shear zone hits the top boundary (Fig. 8b).

*4.2.2. Large sand specimen (smooth boundaries, specimen 320 × 1120 mm², $\lambda_{x1} = 1$, $\lambda_{x2} = 1$, $s_d = 0.05$)*

A large sand specimen of ($320 \times 1120$ mm$^2$) was subject to a similar FE-analysis (Figs. 10 and 11, Table 4). The results are qualitatively the same as for a medium sand specimen (however, their scattering is smaller). For 3 cases, a shear zone hits a top boundary, and the residual normalized vertical force $P/(\sigma_c b_0 l)$ is higher.

The estimated expected value and standard deviations were, respectively: for the peak friction angle $\hat{\phi}_p = 44.22°$ and $\hat{s}_{\phi_p} = 0.37°$, the normalized horizontal displacement of the top boundary $u_1^t/h_0$ corresponding

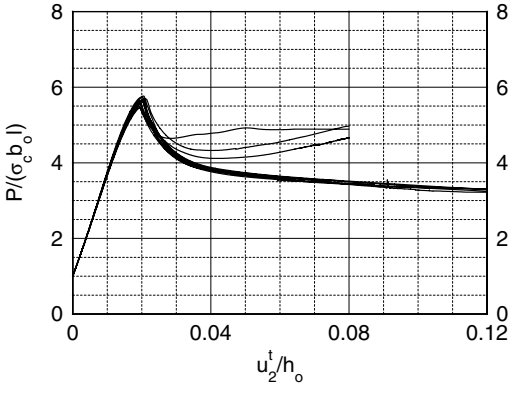


Fig. 10. Evolution of normalized vertical force $P/(\sigma_c b_0 l)$ versus normalized vertical displacement of the upper edge $u_2^t/h_0$ during plane strain compression with a dense specimen for 12 different random fields of $e_0$ ($\bar{e}_0 = 0.60$, specimen size $320 \times 1120$ mm$^2$, smooth boundaries, $\lambda_{x1} = 1$, $\lambda_{x2} = 1$, $s_d = 0.05$).

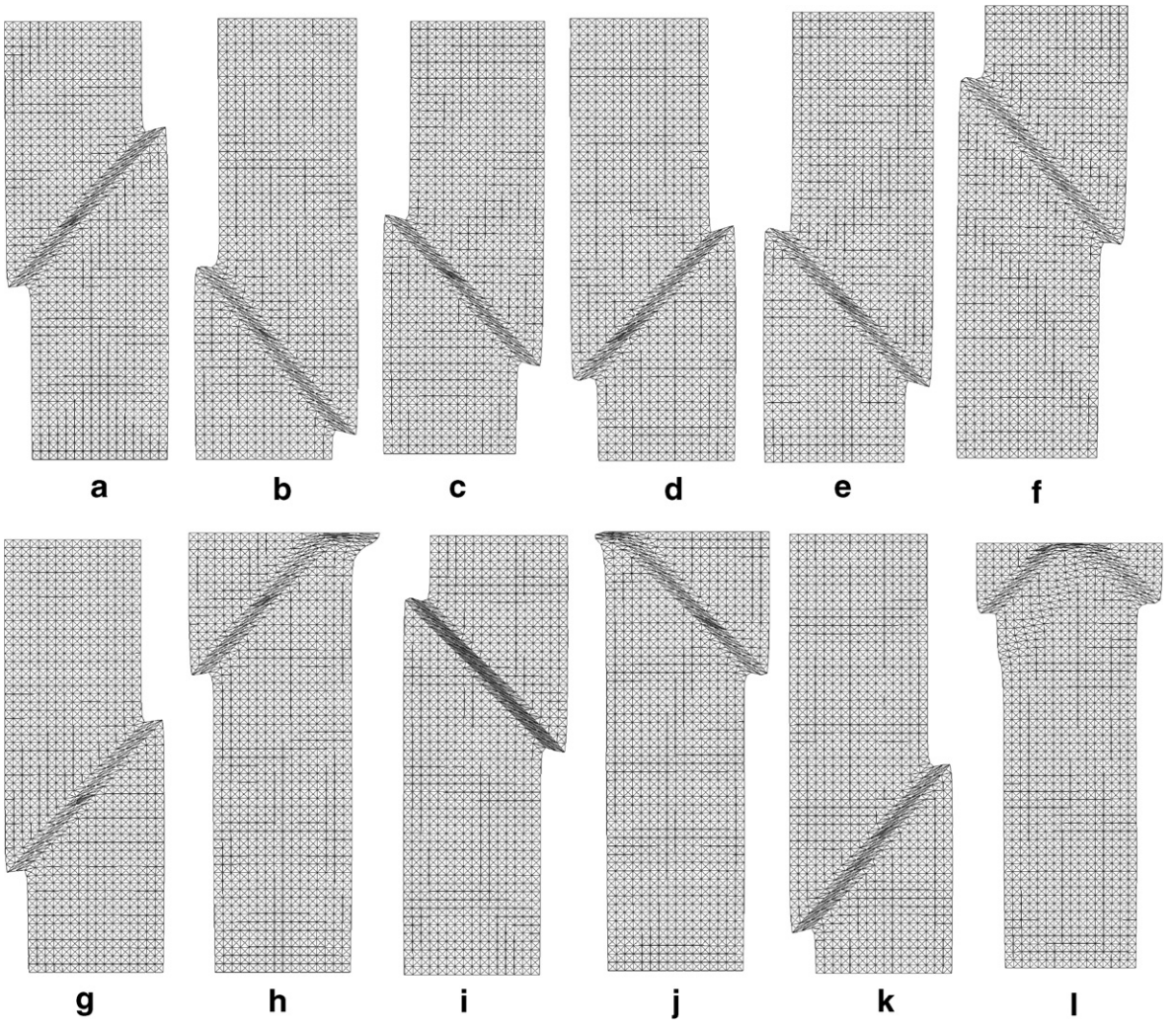


Fig. 11. Deformed FE-mesh with the distribution equivalent total strain measure during compression with a dense specimen for 12 different random fields of $e_0$ ($\bar{e}_0 = 0.60$, specimen size $320 \times 1120\ \mathrm{mm}^2$, smooth boundaries, $\lambda_{x1} = 1$, $\lambda_{x2} = 1$, $s_d = 0.05$).

to the peak $\hat{u}_1^t/h_0 = 0.0020$ and $\hat{s}_{u_1^t}/h_0 = 0.00062$ and the normalized shear zone thickness $\hat{t}_s/d_{50} = 70.3$ and $\hat{s}_{t_s}/d_{50} = 14.59$. The peak friction angle ($\hat{\phi}_p = 44.23°$) is by 1.0° smaller than this with the uniform initial void ratio ($\phi_p = 45.38°$). The shear zone thickness ($t_s/d_{50} = 70$) is larger than with a uniform initial void ratio $t_s/d_{50} = 34$. The residual friction ($\phi_{cr} = 34.5°$ at $u_2^t/h_0 = 7.5\%$) is by 1.5° smaller.

*4.2.3. Medium sand specimen (very rough boundaries, specimen $40 \times 140\ mm^2$, $\lambda_{x1} = 1$, $\lambda_{x2} = 1$, $s_d = 0.05$)*

The results are demonstrated in Figs. 12 and 13 and Table 4 (for the same random fields of $e_0$ as in the case of smooth boundaries).

In all cases, two non-symmetric shear zones appear inside of the specimen. The peak friction angle ($\hat{\phi}_p = 45.24°$) is by 0.5° smaller than with a uniform initial void ratio ($\phi_p = 45.60°$). The shear zone thickness ($t_s/d_{50} = 13.3$) is slightly smaller than this with the uniform initial void ratio $t_s/d_{50} = 14$. The residual friction angle ($\phi_{cr} = 38.77°$ at $u_2^t/h_0 = 10\%$) is smaller by 1.7°.

*4.2.4. Medium sand specimen (smooth boundaries, specimen $40 \times 140\ mm^2$, $\lambda_{x1} = 3$, $\lambda_{x2} = 3$, $s_d = 0.1$)*

The results with a large standard deviation and a weak correlation of $e_0$ are demonstrated in Figs. 14 and 15 and Table 5.

Table 4
The values of peak friction angles $\phi^p$, residual friction angles $\phi_{cr}$, vertical strain corresponding to the maximum vertical force $u_2^t/h_0$, normalized shear zone thickness $t_s/d_{50}$ for different random fields ($\bar{e}_0 = 0.60$, $b_0 = 320$ mm, $h_0 = 1120$ mm, smooth boundaries, $\lambda_{x1} = 1$, $\lambda_{x2} = 1$, $s_d = 0.05$).

| Nr | $\phi^p$ [°] | $\phi_{cr}$ [°] | $u_2^t/h_0$ | $t_s/d_{50}$ |
|---|---|---|---|---|
| B-01 | 44.69 | 32.9 | 0.0200 | 68.4 |
| B-02 | 44.38 | 32.9 | 0.0201 | 45.6 |
| B-03 | 44.34 | 32.7 | 0.0194 | 91.2 |
| B-04 | 44.78 | 32.8 | 0.0205 | 68.4 |
| B-05 | 44.01 | 32.6 | 0.0194 | 68.4 |
| B-06 | 44.53 | 32.8 | 0.0206 | 91.2 |
| B-07 | 43.80 | 32.9 | 0.0191 | 68.4 |
| B-08[a] | 44.49 | 32.7 | 0.0213 | 68.4 |
| B-09 | 44.19 | 32.9 | 0.0201 | 68.4 |
| B-10[a] | 44.22 | 34.3 | 0.0203 | 45.6 |
| B-11 | 43.67 | 33.0 | 0.0195 | 91.2 |
| B-12[a] | 43.61 | 33.4 | 0.0194 | 68.4 |
| Mean value | 44.22 | 33.0 | 0.0200 | 70.3 |
| Uniform distribution of $e_0$ | 45.38 | 34.5 | 0.0229 | 46 |

[a] Shear zone hitting the top boundary.

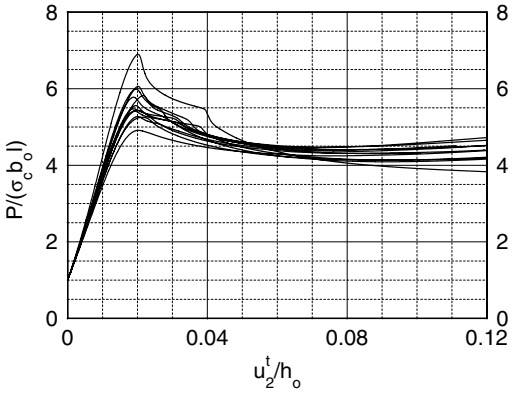


Fig. 12. Evolution of normalized vertical force $P/(\sigma_c b_0 l)$ versus normalized vertical displacement of the upper edge $u_2^t/h_0$ during plane strain compression with a dense specimen for 12 different random fields of $e_0$ ($\bar{e}_0 = 0.60$, specimen size $40 \times 140$ mm$^2$, very rough boundaries, $\lambda_{x1} = 1$, $\lambda_{x2} = 1$, $s_d = 0.05$).

The effect of the random distribution of $e_0$ on the friction angle and shear zone thickness is more pronounced. The peak friction angle ($\hat{\phi}_p = 40.69°$) is by 5° smaller than with a uniform initial void ratio ($\phi_p = 45.62°$). The residual friction angle ($\phi_{cr} = 33.02°$ at $u_2^t/h_0 = 7.5\%$) is smaller by 2°. In all cases, only one shear zone appears inside of the specimen. The shear zone thickness ($t_s/d_{50} = 11.6$) (Table 6) is smaller by 20% than with a uniform initial void ratio ($t_s/d_{50} = 14$) (Table 1).

Finally, the evolution of deformation, void ratio and Cosserat rotation is shown for one selected random field with two intersecting shear zones (medium specimen size of Fig. 13d, very rough boundaries). During deformation, first, a pattern of shear zones can be observed in the specimen (strain localization starts in corners), Fig. 16a. Next, deformation continues to localize within an inclined single shear zone (just before the peak at $u_2^t/h_0 = 2\%$). This shear zone becomes well visible after the peak at $u_2^t/h_0 = 2.1\%$ (Fig. 16c). Next, a second intersecting shear zone occurs at $u_2^t/h_0 = 3.5\%$ (it causes a small jump on the load-displacement curve, Fig. 12). The evolution of deformation is in agreement with experiments (Vardoulakis, 1977, Desrues and Viggiani, 2004). In the specimen region beyond the shear

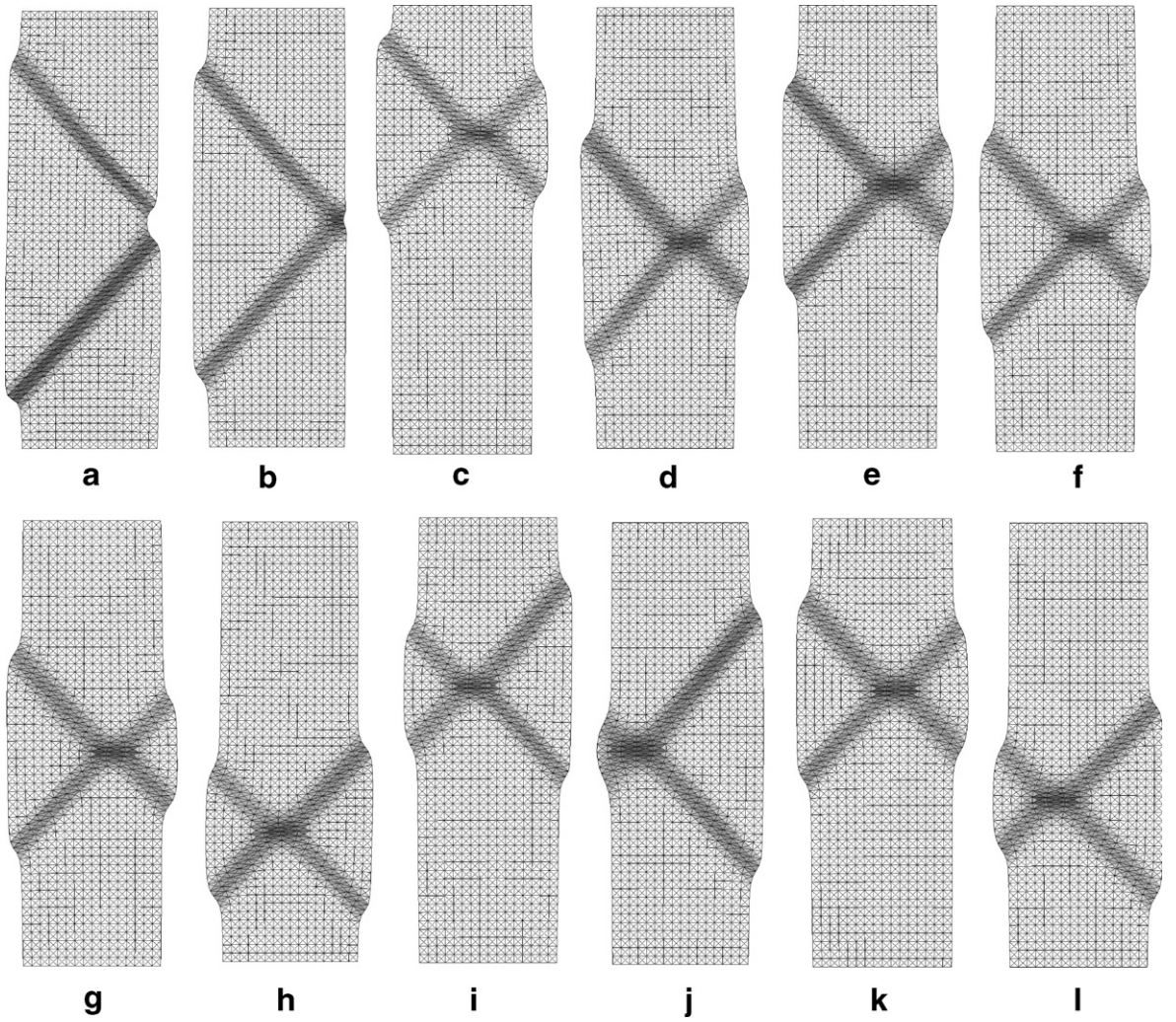


Fig. 13. Deformed FE-mesh with the distribution equivalent total strain measure during compression with a dense specimen for 12 different random fields of $e_0$ ($\bar{e}_0 = 0.60$, specimen size $40 \times 140$ mm$^2$, very rough boundaries, $\lambda_{x1} = 1$, $\lambda_{x2} = 1$, $s_d = 0.05$).

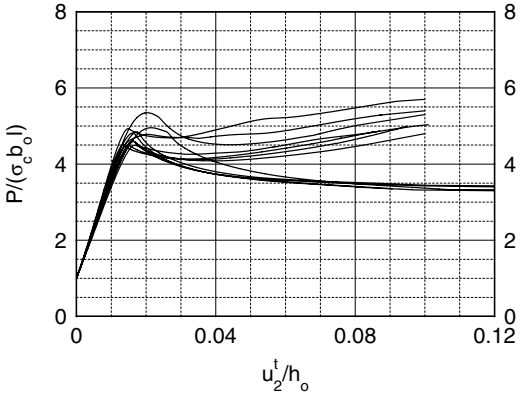


Fig. 14. Evolution of normalized vertical force $P/(\sigma_c b_0 l)$ versus normalized vertical displacement of the upper edge $u_2^t/h_0$ during plane strain compression with a dense specimen for 12 different random fields of $e_0$ ($\bar{e}_0 = 0.60$, specimen size $40 \times 140$ mm$^2$, smooth boundaries, $\lambda_{x1} = 3$, $\lambda_{x2} = 3$, $s_d = 0.10$).

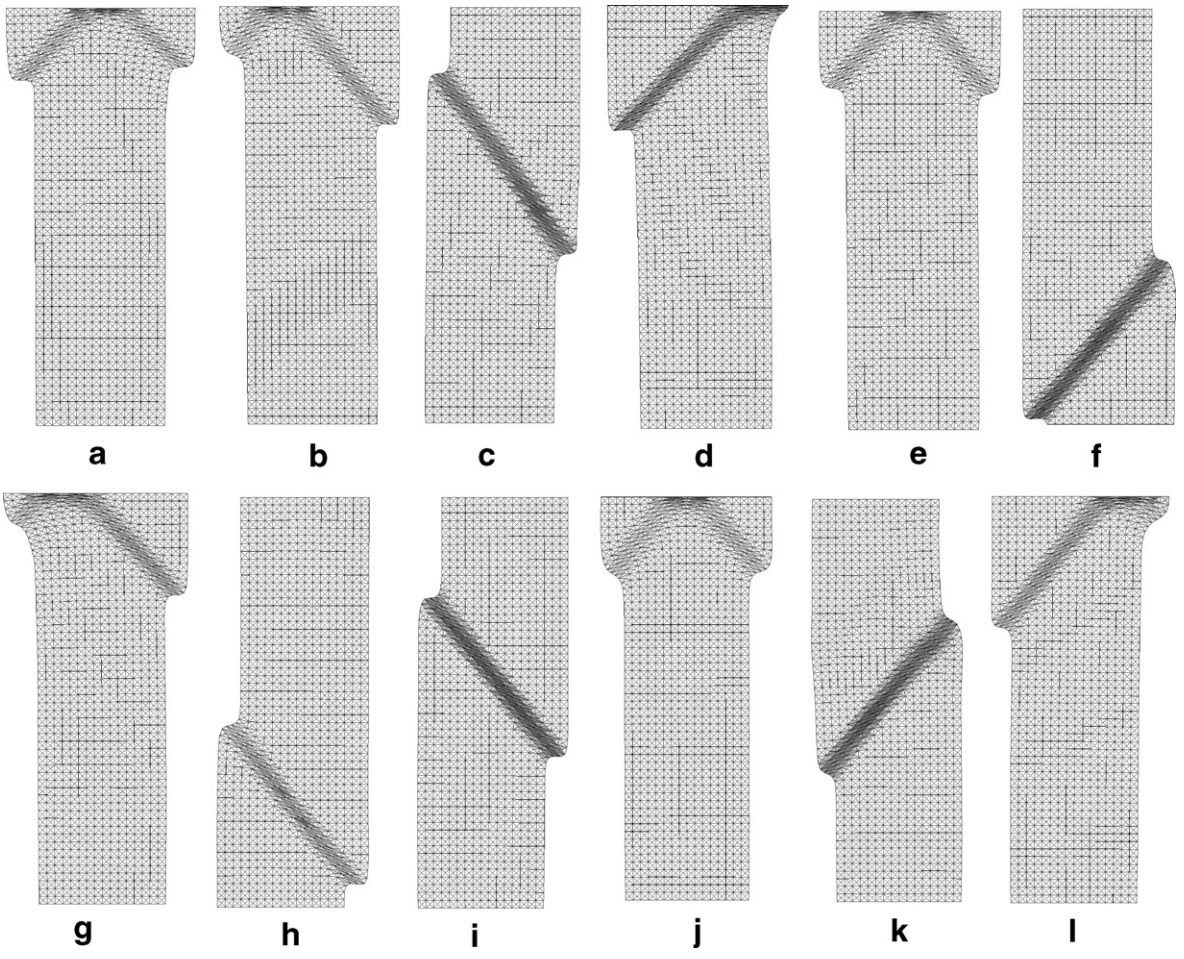


Fig. 15. Deformed FE-mesh with the distribution equivalent total strain measure during compression with a dense specimen for 12 different random fields of $e_0$ ($\bar{e}_0 = 0.60$, specimen size $320 \times 1120$ mm$^2$, smooth boundaries, $\lambda_{x1} = 3$, $\lambda_{x2} = 3$, $s_d = 0.10$).

Table 5
The values of peak friction angles $\phi^p$, residual friction angles $\phi_{cr}$, vertical strain corresponding to the maximum vertical force $u_2'/h_0$, normalized shear zone thickness $t_s/d_{50}$ for different random fields ($\bar{e}_0 = 0.60$, $b_0 = 40$ mm, $h_0 = 140$ mm, very rough boundaries, $\lambda_{x1} = 1$, $\lambda_{x2} = 1$, $s_d = 0.05$)

| Nr | $\phi^p$ [°] | $\phi_{cr}$ [°] | $u_2'/h_0$ | $t_s/d_{50}$ |
|---|---|---|---|---|
| SR-01 | 48.31 | 35.87 | 0.0202 | 11 |
| SR-02 | 45.54 | 37.78 | 0.0196 | 14 |
| SR-03 | 44.82 | 40.57 | 0.0189 | 11 |
| SR-04 | 46.25 | 38.25 | 0.0201 | 14 |
| SR-05 | 43.56 | 39.61 | 0.0198 | 14 |
| SR-06 | 43.71 | 39.52 | 0.0189 | 11 |
| SR-07 | 43.46 | 40.21 | 0.0193 | 14 |
| SR-08 | 44.04 | 37.92 | 0.0196 | 14 |
| SR-09 | 44.98 | 39.58 | 0.0216 | 14 |
| SR-10 | 42.86 | 38.03 | 0.0214 | 14 |
| SR-11 | 42.93 | 38.98 | 0.0201 | 14 |
| SR-12 | 41.43 | 38.96 | 0.0202 | 14 |
| Mean value | 45.24 | 38.77 | 0.0200 | 13.3 |
| Uniform distribution of $e_0$ | 45.60 | 40.4 | 0.0239 | 13 |

Table 6
The values of peak friction angles $\phi^p$, residual friction angles $\phi_{cr}$, vertical strain corresponding to the maximum vertical force $u_2^t/h_0$, normalized shear zone thickness $t_s/d_{50}$ for different random fields ($\bar{e}_0 = 0.60$, $b_0 = 40$ mm, $h_0 = 140$ mm, smooth boundaries, $\lambda_{x1} = 3$, $\lambda_{x2} = 3$, $s_d = 0.10$)

| Nr | $\phi^p$ [°] | $\phi_{cr}$ [°] | $u_2^t/h_0$ | $t_s/d_{50}$ |
|---|---|---|---|---|
| SS-01[a] | 41.50 | 34.80 | 0.0148 | 14 |
| SS-02[a] | 39.55 | 31.87 | 0.0134 | 14 |
| SS-03 | 41.00 | 33.26 | 0.0161 | 14 |
| SS-04[a] | 43.23 | 33.65 | 0.0203 | 11 |
| SS-05[a] | 39.50 | 31.69 | 0.0145 | 14 |
| SS-06 | 41.16 | 33.75 | 0.0173 | 14 |
| SS-07[a] | 40.80 | 33.48 | 0.0204 | 14 |
| SS-08 | 40.05 | 33.47 | 0.0161 | 14 |
| SS-09 | 40.03 | 33.23 | 0.0161 | 11 |
| SS-10[a] | 39.98 | 31.03 | 0.0163 | 17 |
| SS-11 | 39.91 | 33.42 | 0.0215 | 11 |
| SS-12[a] | 41.61 | 32.53 | 0.0167 | 14 |
| Mean value | 40.69 | 33.02 | 0.0170 | 11.6 |
| Uniform distribution of $e_0$ | 45.62 | 34.80 | 0.0236 | 14 |

[a] Shear zone hitting the top boundary.

zone, small changes of void ratio are visible, what is also in agreement with experiments by Yoshida et al. (1994).

## 5. Conclusions

The following conclusions can be drawn from our preliminary non-linear FE-investigations of deterministic and statistical size effects in geometrically similar granular bodies during plane strain compression under constant lateral pressure:

The deterministic size effect (decrease of the shear resistance with increasing specimen size) is insignificant independently of the boundary roughness due to the fact that both the essential features of the material failure and the pressure level are similar. The difference in the peak friction angle is only 0.5°. The residual friction angle is larger for very rough boundaries and does not depend on the specimen size. The rate of material softening strongly decreases with decreasing specimen size. The thickness of the shear zone increases with increasing specimen size (due to a decreasing rate of softening). The number of shear zones depends on the boundary roughness. Two symmetric intersecting shear zones appear inside of the specimen with very rough boundaries and one shear zone with smooth boundaries.

The statistical size effect is significantly stronger than the deterministic one. The mean shear resistance at peak with a stochastic distribution of the initial void ratio is always smaller than with a uniform distribution of the initial void ratio. For a small standard deviation and strongly correlated fields of the initial void ratio in both directions, the difference in the peak internal friction angle at peak and residual state is rather negligible for large and small specimens. In turn, for a large standard deviation and weakly correlated fields in both directions, the difference in the friction angle becomes more pronounced, e.g. 5° (at peak) and 2° (at residual state). This difference is not influenced by the specimen size and boundary roughness.

The location and type of shear localization depends on a stochastic distribution of the initial void ratio and boundary roughness. During deformation, first, a pattern of shear bands can be observed in the sand specimen. Next, deformation continues to localize within a single shear zone (smooth boundaries) or two non-symmetric shear zones (very rough boundaries). The shear zone can hit the top smooth boundary. The mean thickness of the shear zone and its inclination are insignificantly influenced by a stochastic distribution of the initial void ratio.

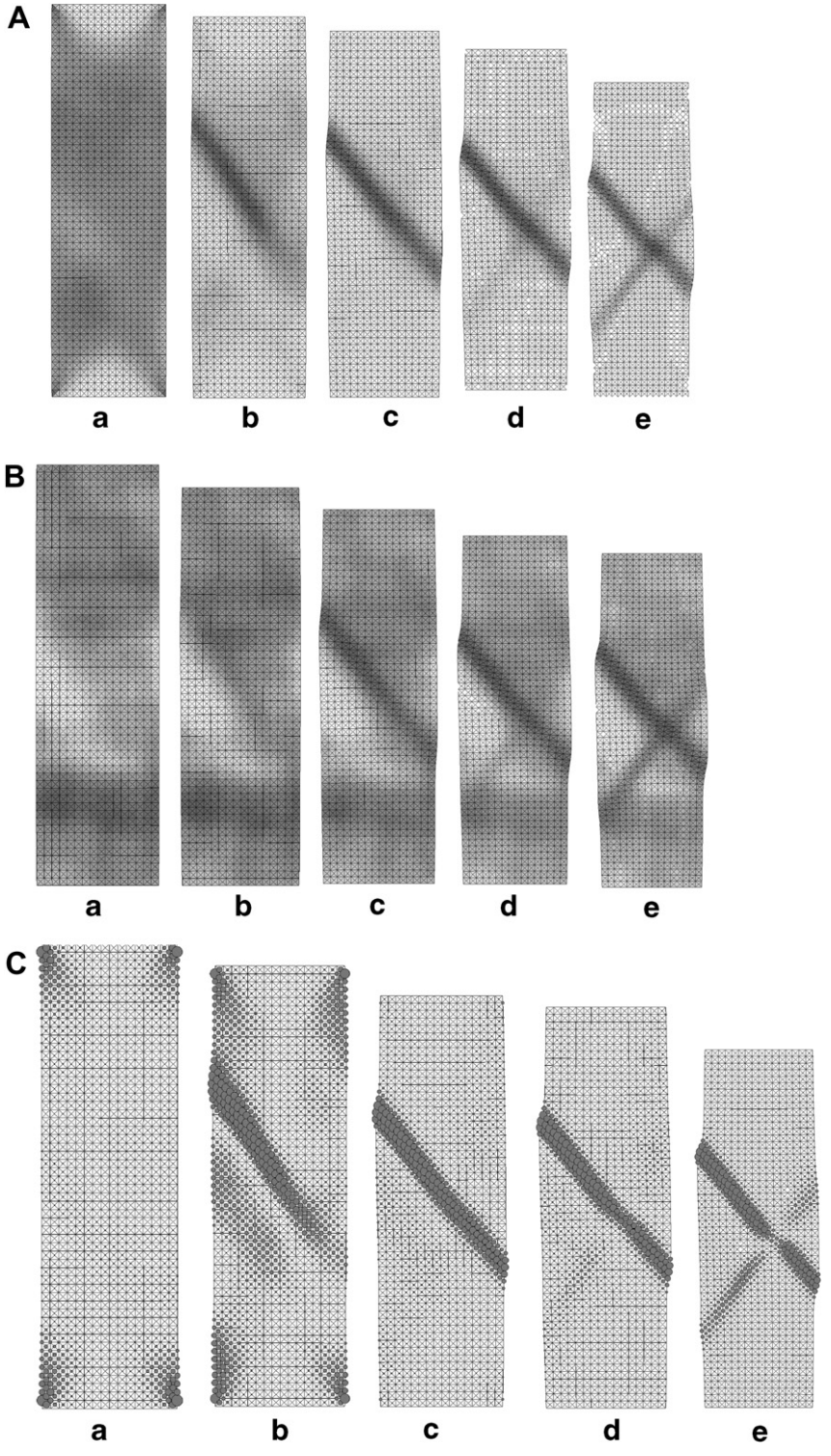


Fig. 16. Evolution of equivalent total strain measure (A), void ratio (B) and Cosserat rotation (C) field during a plane strain compression test (random field of Fig. 13d) at: (a) $u_2'/h_0 = 0.011$, (b) $u_2'/h_0 = 0.021$, (c) $u_2'/h_0 = 0.028$, (d) $u_2'/h_0 = 0.036$, (e) $u_2'/h_0 = 0.042$ ($\bar{e}_0 = 0.60$, very rough boundaries, specimen size $40 \times 140\ \mathrm{mm}^2$).

## References


Bauer, E., 1996. Calibration of a comprehensive hypoplastic model for granular materials. Soils and Foundations 36 (1), 13–26.

Bazant, Z.P., Lin, K.L., 1985. Random creep and shrinkage in structures sampling. Joruanl of Structural Engineering ASCE 111 (5), 1113–1134.

Bazant, Z., Planas, J., 1998. Fracture and Size Effect in Concrete and Other Quasi-brittle Materials. CRC Press LLC.

Bielewicz, E., Górski, J., 2002. Shell with random geometric imperfections. Simulation-based approach. International Journal of Non-linear Mechanics 37 (4–5), 777–784.

Darve, F., Flavigny, E., Megachou, M., 1995. Yield surfaces and principle of superposition revisited by incrementally non-linear constitutive relations. International Journal of Plasticity 11 (8), 927–948.

Desrues, J., Chambon, R., 1989. Shear band analysis for granular materials – the question of incremental linearity. Ingenieur Archiv 59, 187–196.

Desrues, J., Viggiani, C., 2004. Strain localization in sand: overview of the experiments in Grenoble using stereophotogrammtery. Journal of Numerical and Analytical Methods in Geomechanics 28 (4), 279–321.

Ehlers, W., Graf, T., 2003. Adaptive computation of localization phenomena in geotechnical applications. In: Labuz, J., Drescher, A. (Eds.), Bifurcations and Instabilities in Geomechanics. Swets and Zeitlinger, pp. 247–262.

Florian, A., 1992. An efficient sampling scheme: updated latin hypercube sampling. Probabilistic Engineering Mechanics 2, 123–130.

Gudehus, G., 1996. Comprehensive constitutive equation for granular materials. Soils and Foundations 36 (1), 1–12.

Gudehus, G., Nübel, K., 2004. Evolution of shear bands in sand. Geotechnique 113 (54(3)), 187–201.

Gudehus, G., 2006. Seismo-hypoplasticity with a granular temperature. Granular Matter 8, 93–102.

Herle, I., Kolymbas, D., 2004. Hypoplasticity for soils with low friction angles. Computers and Geotechnics 31, 365–373.

Górski, J., 2006. Non-linear models of structures with random geometric and material imperfections–simulation-based approach. Gdansk University of Technology, 68.

Groen, A.E., 1997. Three-dimensional elasto-plastic analysis of soils. PhD Thesis, Delft University, pp. 1-114.

Gutierrez, M.A., de Borst, R., 1998. Energy dissipation, internal length scale and localization patterning – a probabilistic approach. In: Idelsohn, S., Onate, E., Dvorkin, E. (Eds.), Computational Mechanics. CIMNE, Barcelona, pp. 1–9.

Gutierrez, M.A., 2006. Size sensitivity for the reliability index in stochastic finite element analysis of damage. International Journal of Fracture 137 (1-4), 109–120.

Hattamleh, O. Al., Muhunthan, B., Zbib, H.M., 2005. Stress distribution in granular heaps using multi-slip formulation. Intern. Journal for Numerical and Analytical Methods in Geomechanics 29, 713–727.

Herle, I., Gudehus, G., 1999. Determination of parameters of a hypoplastic constitutive model from properties of grain assemblies. Mechanics of Cohesive-Frictional Materials 4 (5), 461–486.

Hurtado, J.E., Barbat, A.H., 1998. Monte Carlo techniques in computational stochastic mechanics. Archives of Computational Method in Engineering 5 (1), 3–30.

Knabe, W., Przewłócki, J., Rózyński, G., 1998. Spatial averages for linear elements for two-parameter random field. Probabilistic Engineering Mechanics 13 (3), 147–167.

Kolymbas, D., 1977. A rate-dependent constitutive equation for soils. Mechanics Research Communication 6, 367–372.

Lade, P.V., 1977. Elasto-plastic stress–strain theory for cohesionless soil with curved yield surfaces. International Journal of Solid Structures 13, 1019–1035.

Maier, T., 2002. Numerische Modellierung der Entfestigung im Rahmen der Hypoplastizität. PhD Thesis, University of Dortmund.

Masin, D., 2005. A hypoplastic constitutive model for clays. International Journal of Numerical and Analytical Methods in Geomechanics 29, 311–336.

Mühlhaus, H.-B., 1990. Continuum models for layered and blocky rock. In: Hudson, J.A., Fairhurst, Ch. (Eds.), . In: Comprehensive Rock Engineering, vol. 2. Pergamon, pp. 209–231.

Niemunis, A., Herle, I., 1997. Hypoplastic model for cohesionless soils with elastic strain range. Mechanics of Cohesive-Frictional Materials 2, 279–299.

Niemunis, A., 2003. Extended hypoplastic models for soils. In: Habilitation Monography. Gdansk University of Technology.

Niemunis, A., Wichtmann, T., Petryna, Y., Triantafyllidis, T., 2005. Stochastic modeling of settlements due to cyclic loading for soil-structure interaction. In: Proc. Int. Conf. Structural Damage and Lifetime Assessment, Rome.

Oda, M., 1993. Micro-fabric and couple stress in shear bands of granular materials. In: Thornton, C. (Ed.), Powders and Grains. Balkema, Rotterdam, pp. 161–167.

Pasternak, E., Mühlhaus, H.-B., 2001. Cosserat continuum modelling of granulate materials. In: Valliappan, S., Khalili, N. (Eds.), Computational Mechanics – New Frontiers for New Millennium. Elsevier Science, pp. 1189–1194.

Pestana, J.M., Whittle, A.J., 1999. Formulation of a unified constitutive model for clays and sands. Journal of Numerical and Analytical Methods in Geomechanics 23, 1215–1243.

Przewłócki, J., Górski, J., 1999. Stochastic FEM analysis of strip foundation. TASK Quarterly 3 (2), 173–181.

Przewłócki, J., Górski, J., 2001. Strip foundation on 2-D and 3-D random subsoil. Probabilistic Engineering Mechanics 16, 121–136.

Regueiro, R.A., Borja, R.I., 2001. Plane strain finite element analysis of pressure sensitive plasticity with strong discontinuity. International Journal of Solids and Structures 38 (21), 3647–3672.

Schäfer, H., 1962. Versuch einer Elastizitätstheorie des zweidimensionalen ebenen Cosserat–Kontinuums. Miszellaneen der Angewandten Mechanik, Festschrift Tolmien, W., Akademie-Verlag, Berlin.

Tamagnini, C., Viggiani, C., Chambon, R., 2000. A review of two different approaches to hypoplasticity. In: Kolymbas, D. (Ed.), Constitutive Modeling of Granular Materials. Heidelberg, Berlin, pp. 107–145.
Tatsuoka, F., Goto, S., Tanaka, T., Tani, K., Kimura, Y., 1997. Particle size effects on bearing capacity of footing on granular material. In: Asaoka, A., Adachi, T., Oka, F. (Eds.), Deformation and Progressive Failure in Geomechanics. Pergamon, pp. 133–138.
Tejchman, J., Wu, W., 1993. Numerical study on shear band patterning in a Cosserat continuum. Acta Mechanica 99, 61–74.
Tejchman, J., Bauer, E., 1996. Numerical simulation of shear band formation with a polar hypoplastic model. Computers and Geotechnics 19 (3), 221–244.
Tejchman, J., Herle, I., 1999. A "class A" prediction of the bearing capacity of plane strain footings on granular material. Soils and Foundations 39 (5), 47–60.
Tejchman, J., Gudehus, G., 2001. Shearing of a narrow granular strip with polar quantities. Journal of Numerical and Analytical Methods in Geomechanics 25, 1–18.
Tejchman, J., 2004a. FE-simulations of a direct wall shear box test. Soils and Foundations 44 (4), 67–81.
Tejchman, J., 2004b. Influence of a characteristic length on shear zone formation in hypoplasticity with different enhancements. Computers and Geotechnics 31 (8), 595–611.
Tejchman, J., Niemunis, A., 2006. FE-studies on shear localization in an anisotropic micro-polar hypoplastic granular material. Granular Matter 8 (3-4), 205–220.
Tejchman, J., Bauer, E., Wu, W., 2007. Effect of texturial anisotropy on shear localization in sand during plane strain compression. Acta Mechanica 1-4, 23–51.
Tejchman, J., Górski, J., 2007a. Deterministic and statistical size effect during shearing of granular layer within a micro-polar hypoplasticity. International Journal of Numerical and Analytical Methods in Geomechanics (in press).
Tejchman, J., Górski, J., 2007b. Investigations of size effects in granular bodies during plane strain compression. Lecture Notes in Complex Systems (in press).
Vanmarcke, E.-H., 1983. Random Fields: Analysis and Synthesis. MIT Press, Cambridge.
Vardoulakis, I., 1977. Scherfugenbildung in Sandkörpern als Verzweigungsproblem. PhD thesis, Institute for Soil and Rock Mechanics, University of Karlsruhe, 70.
Vardoulakis, I., Goldscheider, M., Gudehus, G., 1978. Formation of shear bands in sand bodies as a bifurcation problem. International Journal of Numerical and Analytical Methods in Geomechanics 2, 99–128.
Vermeer, P., 1982. A five-constant model unifying well-established concepts. In: Gudehus, G., Darve, F., Vardoulakis, I. (Eds.), Proc. Int. Workshop on Constitutive Relations for Soils. Balkema, pp. 175–197.
Walukiewicz, H., Bielewicz, E., Górski, J., 1997. Simulation of nonhomogeneous random fields for structural applications. Computers and Structures 64 (1-4), 491–498.
Wang, C.C., 1970. A new representation theorem for isotropic functions. Journal of Rational Mechanics and Analysis 36, 166–223.
Weibull, W., 1951. A statistical theory of the strength of materials. Journal of Applied Mechanics 18 (9), 293–297.
Wernick, E., 1978. Tragfähigkeit zylindrischer Anker in Sand unter besonderer Berücksichtigung des Dilatanzverhaltens. In: Publication Series of the Institute for Rock and Soil Mechanics. University Karlsruhe, 75.
von Wolffersdorff, P.A., 1996. A hypoplastic relation for granular materials with a predefined limit state surface. Mechanics Cohesive-Frictional Materials 1, 251–271.
Wu, W., 1992. Hypoplastizität als mathematisches Modell zum mechanischen Verhalten granularer Stoffe. In: Publication Series of the Institute of Soil and Rock Mechanics. University Karlsruhe, 129.
Wu, W., Kolymbas, D., 2000. Hypoplasticity then and now. In: Kolymbas, D. (Ed.), Constitutive Modeling of Granular Materials. Springer, Heidelberg, pp. 57–105.
Yoshida, T., Tatsuoka, F., Siddiquee, M., 1994. Shear banding in sands observed in plane strain compression. In: Chambon, R., Desrues, J., Vardoulakis, I. (Eds.), Localisation and Bifurcation Theory for Soils and Rocks. Balkema, Rotterdam, pp. 165–181.